# On the Kármán–Pohlhausen Momentum-Integral Approach.
# Extension to Flow Over a Cylinder with a Variable Pressure Gradient

Rudy Al Ahmar*[ORCID] and Joseph Majdalani†[ORCID]

*Auburn University, Auburn, AL 36849*

In this work, the Kármán–Pohlhausen (KP) momentum-integral approach based on optimized fourth-order (MX4) polynomial approximations of the velocity and temperature profiles is applied to a classical benchmark problem, namely, that of a cylinder in crossflow with a variable pressure gradient. This enables us to extract closed-form expressions for both hydrodynamic and thermal boundary-layer parameters and then compare the newly found solutions to their counterparts obtained using Pohlhausen's cubic (KP3) and quartic (KP4) polynomials. As usual, the farfield around the cylinder is modeled using potential flow theory and the momentum-integral analysis is paired with Walz's empirical expression for the momentum thickness, which is based on a wide collection of experiments. This procedure permits retrieving explicit relations for the pressure-sensitive KP3, KP4, and MX4 velocity profiles across the boundary layer; one also obtains accurate approximations for the pressure distribution around the cylinder as well as an improved prediction of the separation point, namely, to within 0.87% of the actual location. In this process, refined estimates are produced for several characteristic parameters whose distributions are found to be in favorable agreement with experimental measurements and numerical simulations. These include the disturbance, momentum, and displacement thicknesses as well as the skin friction, pressure, and total drag coefficients. Lastly, the thermal analysis is undertaken using both isothermal and isoflux boundary conditions. For each of these cases, closed-form analytical solutions are obtained for the local Nusselt number distribution around the cylinder, and these distributions are found to exhibit noticeably reduced errors relative to their classical values.

## Nomenclature

| | |
|---|---|
| $C_D$ | total drag coefficient |
| $C_{D_p}$ | pressure drag coefficient |
| $C_f, C_{D_f}$ | local and total skin friction drag coefficient |
| $c_p$ | constant pressure specific heat |
| $C_P$ | pressure coefficient |
| $D$ | cylinder diameter |
| $h$ | convective heat transfer coefficient |
| $k_f$ | fluid thermal conductivity |
| $Nu_D$ | Nusselt number |
| $p$ | pressure |
| $Pr$ | Prandtl number |
| $q$ | heat flux density per unit area |
| $Re_D$ | Reynolds number |
| $T$ | temperature |
| $u$ | tangential velocity in the $x$ direction |
| $U(x)$ | local farfield potential flow velocity |
| $U_\infty$ | approaching freestream velocity |
| $v$ | normal velocity in the $y$ direction |
| $x$ | tangential coordinate along cylindrical surface |
| $y$ | normal component above cylindrical surface |

*Greek*

| | |
|---|---|
| $\alpha$ | thermal diffusivity |
| $\delta$ | hydrodynamic boundary-layer disturbance thickness |
| $\delta^*$ | displacement thickness |

---

*Graduate Research Assistant, Department of Aerospace Engineering, Member AIAA.

†Professor and Francis Chair, Department of Aerospace Engineering, Associate Fellow AIAA.

| | |
|---|---|
| $\delta_T$ | thermal boundary-layer thickness |
| $\Lambda$ | Pohlhausen's pressure-gradient parameter |
| $\mu, \rho$ | fluid molecular viscosity and density |
| $\nu$ | kinematic viscosity, $\mu/\rho$ |
| $\phi$ | azimuthal angle measured from stagnation point (ccw) |
| $\phi_{\text{sep}}$ | azimuthal angle at flow separation point |
| $\theta$ | momentum thickness |
| $\tau_w$ | wall shear stress |
| $\xi$ | normalized $y$ coordinate (hydrodynamic), $y/\delta$ |
| $\xi_T$ | normalized $y$ coordinate (thermal), $y/\delta_T$ |

# I. Introduction

$\mathbf{M}$ODERN boundary-layer analysis may be traced back to a highly impactful 1904 paper by Prandtl [1] in which a reduced partial differential set of the Navier–Stokes equations is provided for the treatment of viscous flow problems. Four years later, this significant development in aerodynamics is succeeded by a brilliantly constructed similarity solution for flow over a flat plate by Prandtl's first doctoral student, Blasius [2]. Then, in 1921, a seemingly straightforward extension to Prandtl's equations is conceived in the form of an integral formulation, again this time, by two of Prandtl's most celebrated students. After its introduction through two sequential papers by von Kármán [3] and Pohlhausen [4], the so-called Kármán–Pohlhausen (KP) momentum-integral approach may be seen to quickly gain popularity within the aerodynamics, fluid mechanics, and propulsion communities. In hindsight, this may be attributed to its versatility, simplicity, and effectiveness at capturing both laminar and turbulent boundary layers in a variety of phenomenological problems. In fact, given its broad applicability range, this method is presently featured in several textbooks on the subject including those by Oleinik and Samokhin [5], Schetz and Bowersox [6], Pritchard and Mitchell [7], Schlichting and Gersten [8], and White and Majdalani [9]; it is also cited or used at the basis of several interesting studies such as those by Cantwell [10], Khan et al. [11], Bujurke and Jagadeeswar [12], and others. More contemporaneously, it has been relied upon to predict the viscous drag in modern computational schemes based on potential flow solvers and surface vorticity panel codes such as FlightStream® by DiMaggio et al. [13].

To begin, it may be instructive to note that, from a procedural standpoint, Kármán's momentum-integral approach is predicated on the availability of suitable representations of the velocity profile in the nearfield. In fact, the systematic construction of a viable profile is addressed quite elegantly in a 1921 companion paper by Pohlhausen [4]. For this reason, the overarching method is presently referred to as "KP's," namely, in recognition of both contributors, whose centennial articles we celebrate.

Pohlhausen's idea is simple. By postulating reasonable boundary conditions that can be applied at the extremities of a viscous region, velocity profiles of increasing orders can be methodically developed. These are often termed P2, P3, and P4, in reference to their quadratic, cubic, or quartic orders[14]. Naturally, higher-order approximations are capable of satisfying a larger number of postulated conditions. Most perplexingly, however, as Pohlhausen's polynomial orders are elevated, their ability to predict basic boundary-layer characteristics has been shown to deteriorate. Instead of producing a reduced error at successively increasing orders, a magnification in the error is realized[7–9]. For example, the errors in predicting the displacement thickness and shape factor for planar flow over a flat plate increase from 4.7% and 7.2% to 12% and 17% when P4 is used in lieu of P3[9]. Effectively, to overcome the inexplicable increase in error, several other methods are later developed and these include two comparable formulations by Walz [15] and Thwaites [16]. The latter consist of semi-empirical integral relations that predict the momentum thickness directly from the velocity profile in the farfield region irrespective of the flow developing in the nearfield. As such, these alternative techniques provide no particular detail on the velocity or temperature profiles across the viscous or thermal layers.

In actuality, due to the findings reported in a recent study by Majdalani and Xuan [17], the paradoxical error behavior undermining Pohlhausen's polynomials is rationally explained. This is accomplished by demonstrating that one of the postulated boundary conditions by Pohlhausen, which drastically affects polynomials of order four and higher, is rather imprecise, being markedly dissimilar from its numerically computed value. It is then shown that, by relaxing the second-order curvature requirement postulated by Pohlhausen on the velocity at the edge of the viscous layer, a substantially improved quartic polynomial representation is achieved [17]. More specifically, this is accomplished by replacing the deficient condition with an optimal slope at the wall to the extent of reducing the predictive error accrued in the KP formulation by one full order of magnitude.

American Institute of Aeronautics and Astronautics

Having demonstrated the effectiveness of this novel approach in modeling the motion over a flat plate with a zero pressure gradient [17], it is the purpose of this work to extend its application to another canonical problem, namely, that of a circular cylinder in crossflow [18]. In this geometric setting, the decreasing and then increasing flow area normal to the uniform stream past the nose section of the cylinder leads to a pressure gradient that must be accounted for. From a practical perspective, the analysis of flow past a cylinder remains of tremendous academic interest due, partially, to its ubiquitous coverage in textbooks on the subject [5–9] and, partially, to its frequent designation as a benchmark problem in the development of new computational techniques [19]. In fact, the characterization of flow development around bluff bodies in general and circular cylinders in particular remains an active area of research that continues to attract dedicated experimental [20–23] and computational [24–33] studies.
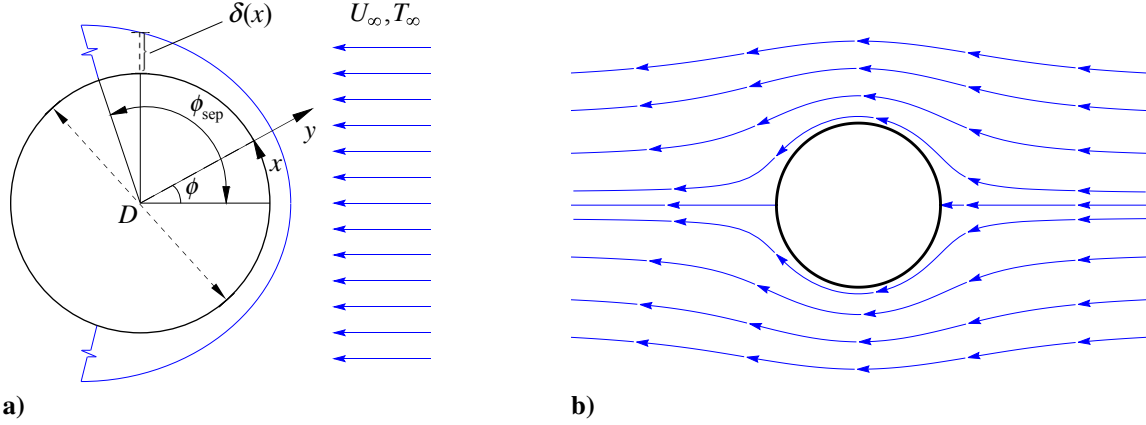
Naturally, the spatial variations of the pressure gradient and farfield velocity around the cylinder give rise to additional complexities in the momentum equation relative to the flat-plate problem at zero angle of incidence [17]. The present extension from a flat plate to a cylinder in crossflow using an optimized quartic polynomial approximation is therefore essential to pursue in order to ascertain the manner by which the presence of a pressure gradient can be judiciously handled. This will be attempted while taking into account the results obtained by Khan et al. [34] for the boundary-layer treatment of a cylinder in crossflow. The latter is carried out using Pohlhausen's quartic velocity profile [3] in conjunction with the method of Walz [15] to extract analytical expressions for a variety of viscous and thermal boundary-layer properties. To prove its effectiveness, an optimized quartic polynomial, which is based on a slightly refined momentum-integral formulation [17], will be introduced and shown to outperform in its predictive capability both cubic (KP3) and quartic (KP4) Pohlhausen polynomials.

From an organizational standpoint, the article is divided into two main sections augmenting the present introduction and concluding material of Sec. IV. The first part focuses on the hydrodynamic momentum analysis of the viscous boundary-layer structure over a cylinder in crossflow. This is undertaken in Sec. II using Kármán–Pohlhausen's both cubic (KP3) and quartic (KP4) flow profiles as well as an improved quartic (MX4) polynomial approximation of the nearfield [17]. In all three cases, the farfield is represented by the classic potential flow solution and all results are compared to existing numerical and experimental measurements. In this process, the momentum-thickness estimation is retrieved from the well-established integral formulation by Walz [15]. Results based on the MX4 solution are then shown to be the most precise at forecasting the disturbance, displacement, and momentum thicknesses as well as the separation point along the rear portion of the cylinder. Because of its unique characteristics relative to its counterparts, the MX4 solution is also seen to predict the most accurate location of the maximum skin friction coefficient along the surface. In the second part, the main focus is shifted to the thermal boundary layer and heat transfer analyses of the same problem using both isothermal and isoflux surface conditions. This is undertaken in Sec. III where both traditional KP3 and KP4 as well as the improved polynomial approximation MX4 are implemented in conjunction with the Reynolds analogy, namely, to characterize the thermal boundary-layer structures and corresponding Nusselt number relations. The underlying effort is performed for a total assortment of six cases that consider three different KP3, KP4, and MX4 temperature profiles and both isothermal and isoflux surface conditions. Here too, all predictions are compared to one another and to existing empirical correlations. In this process, the closed-form analytical expressions associated with the improved MX4 profile are shown to be the most accurate at estimating the thermal characteristics irrespective of whether a constant wall temperature or heat flux condition is prescribed.

## II. Hydrodynamic Analysis

### A. Problem Formulation and Governing Equations

We consider a two-dimensional circular cylinder of diameter $D$ and infinite width, which is surrounded by an incompressible Newtonian fluid approaching at uniform axial speed $U_\infty$ and temperature $T_\infty$. As depicted in Fig. 1a, $x$ stands for the circular arc distance measured tangentially along the surface of the cylinder, $y$ refers to the normal distance at any station $x$, $\phi$ denotes the azimuthal angle measured counterclockwise from the front stagnation point at the nose of the cylinder, and $\delta(x)$ represents the boundary-layer disturbance thickness. Using the subscript "sep" to abbreviate the term "separation," our domain of interest ranges from $\phi = 0°$ at $x = 0$ to the point of separation at $\phi = \phi_{sep}$ or $x_{sep} = \phi_{sep}D/2$. The potential flow solution for the farfield, which extends beyond the edge of the viscous layer, can be suitably represented by $U(x) = 2U_\infty \sin \phi$, as illustrated in Fig. 1b [9]; therein, the characteristic streamlines of the inviscid outer solution are outlined. In the nearfield, one may follow Prandtl [1] by implementing an order-of-magnitude scaling analysis through which terms of lower order can be systematically dismissed. Using standard notation, the reduced set of Navier–Stokes equations, which form the backbone of the substantially simplified

American Institute of Aeronautics and Astronautics

**Fig. 1. Side-by-side schematics of a) an infinitely long cylinder in a crossflow configuration identifying the growing disturbance thickness and principal coordinates in the presence of uniform flow in the farfield with speed $U_\infty$ and temperature $T_\infty$, and b) streamlines corresponding to the idealized, slip-permitting, potential solution denoting the farfield region.**

boundary-layer equations, can be written as:

$$\frac{\partial u}{\partial x} + \frac{\partial v}{\partial y} = 0 \qquad \text{(continuity)}, \qquad (1)$$

$$u\frac{\partial u}{\partial x} + v\frac{\partial u}{\partial y} = -\frac{1}{\rho}\frac{\mathrm{d}p}{\mathrm{d}x} + \nu\frac{\partial^2 u}{\partial y^2} \qquad \text{(wall-tangential $x$-momentum equation)}, \qquad (2)$$

$$\frac{\mathrm{d}p}{\mathrm{d}y} = 0 \qquad \text{(wall-normal $y$-momentum equation)}, \qquad (3)$$

$$u\frac{\partial T}{\partial x} + v\frac{\partial T}{\partial y} = \alpha\frac{\partial^2 T}{\partial y^2} \qquad \text{(energy equation)}, \qquad (4)$$

where $(\rho, p, T)$ and $(u, v)$ denote the density, pressure, temperature, and both axial and normal velocity components within the boundary-layer region, whereas $\nu$ and $\alpha$ stand for the viscous and thermal diffusivity coefficients, respectively.

Four years after the advent of these equations, and pursuant to Prandtl's milestone achievement, Blasius [2] manages to extract a nearly exact shape-preserving similarity solution for the incompressible motion over a flat plate at zero incidence. By demonstrating that the second-order viscous diffusion term in the wall-normal direction trumps its counterpart in the wall-tangential direction, and through the use of a brilliant similarity transformation, Blasius reduces Eqs. (1–3) to a third-order differential equation that can be solved numerically. For the reader's convenience, this equation may be expressed in terms of the normalized velocity profile, $F(\xi) \equiv u/U$, when written as:

$$F'''F' - F''^2 + \tfrac{1}{2}a^2 F'^2 F = 0, \quad \text{with} \quad F(0) = F''(0) = 0, \quad \text{and} \quad F(\infty) = 1, \qquad (5)$$

where $\xi \equiv y/\delta$ denotes the normalized boundary-layer coordinate in lieu of the Blasius similarity variable (see Appendix A for detail). In 1921, an alternative integral technique to these equations is introduced by von Kármán [3], thus leading to the momentum-integral formulation, particularly, whose centennial we recognize in this Special Collection. The latter is actually applied straightforwardly in a companion article by Pohlhausen [4] to showcase its effectiveness at capturing the various boundary-layer properties for flow over a flat plate. This is carried out in conjunction with the use of polynomial approximations to represent the velocity profile across the viscous region. In short, as detailed by Schlichting and Gersten [8], the incompressible form of the momentum-integral equation can be written as:

$$\frac{C_f}{2} \equiv \frac{\tau_w}{\rho U^2} = \frac{1}{U^2}\frac{\partial}{\partial t}\left(U\delta^*\right) + \frac{\mathrm{d}\theta}{\mathrm{d}x} + \left(2\theta + \delta^*\right)\frac{1}{U}\frac{\mathrm{d}U}{\mathrm{d}x} \qquad \text{(momentum-integral equation)}, \qquad (6)$$

where $C_f$, $\tau_w$, $\delta^*$, and $\theta$ stand for the skin friction coefficient, wall shear stress, displacement thickness, and momentum thickness, respectively. The last two properties along with their ratio, which returns the shape factor $H \equiv \delta^*/\theta$, can be

4

American Institute of Aeronautics and Astronautics

evaluated from

$$\delta^* \equiv \int_0^\infty \frac{U-u}{U}\,\mathrm{d}y \approx \delta \int_0^1 (1-F)\,\mathrm{d}\xi, \tag{7}$$

and

$$\theta \equiv \int_0^\infty \frac{u}{U}\frac{U-u}{U}\,\mathrm{d}y \approx \delta \int_0^1 F(1-F)\,\mathrm{d}\xi, \tag{8}$$

with

$$H \equiv \frac{\int_0^\infty \frac{U-u}{U}\,\mathrm{d}y}{\int_0^\infty \frac{u}{U}\frac{U-u}{U}\,\mathrm{d}y} \approx \frac{\int_0^1 (1-F)\,\mathrm{d}\xi}{\int_0^1 F(1-F)\,\mathrm{d}\xi}. \tag{9}$$

Given our interest in pursuing steady-state solutions, we may eliminate the time-dependent terms in Eq. (6) and continue our analysis by referring to

$$\frac{C_f}{2} = \frac{\mathrm{d}\theta}{\mathrm{d}x} + (2+H)\frac{\theta}{U}\frac{\mathrm{d}U}{\mathrm{d}x} \qquad \text{(steady momentum-integral equation)}. \tag{10}$$

## B. Flow Regime and Boundary Conditions

In the laminar boundary-layer regime, the local Reynolds number $Re_x$ may be assumed to be reasonably small, specifically, not exceeding the critical value of $10^5$. Moreover, in the presence of a uniform crossflow velocity, the viscous disturbance thickness begins to grow from its thinnest value at the stagnation point ($\phi = 0°$) to a maximum height that occurs at separation. As illustrated in Fig. 1a, the latter takes place along the aft portion of the cylinder. Then, considering the typically small size of the boundary-layer thickness compared to the cylindrical radius, the flow bending effect may be neglected in a leading-order approximation. As such, the tangential motion along the curved surface may be likened to that of its axial counterpart over a flat plate [35]. This simple analogy enables us to employ the same set of flow profiles devised by Pohlhausen [4] and others to model the velocity distribution within the boundary-layer region using the KP approach [3]. Some of these formulations are reviewed by Majdalani and Xuan [17] and further discussed by Pritchard and Mitchell [7]. In short, the guessed profiles consist of several piecewise approximations that are intended to mimic the behavior of the Blasius solution over the $0 \le y \le \delta$ interval, and that become fixed at unity over the semi-infinite domain, $\delta < y < \infty$. In the absence of a pressure gradient, three of these profiles are of particular interest here. These consist of Pohlhausen's cubic and quartic profiles [4],

$$\frac{u}{U} = \frac{3}{2}\frac{y}{\delta} - \frac{1}{2}\frac{y^3}{\delta^3} \quad \text{(P3)} \quad \text{and} \quad \frac{u}{U} = 2\frac{y}{\delta} - 2\frac{y^3}{\delta^3} + \frac{y^4}{\delta^4} \quad \text{(P4)}, \tag{11}$$

which are often referred to as P3 and P4, in reference to their polynomial orders [14], as they satisfy either four or five of the basic boundary conditions postulated by Pohlhausen [4]. Using similar arguments to those made by Pohlhausen [4], and by avoiding a prematurely imposed boundary condition on the normal shear-stress gradient evaluated at the edge of the boundary layer, a rationally-optimized quartic profile is derived by Majdalani and Xuan [17]. Again, for the case of zero angle of incidence over a flat plate, one gets:

$$\frac{u}{U} = \frac{5}{3}\frac{y}{\delta} - \frac{y^3}{\delta^3} + \frac{1}{3}\frac{y^4}{\delta^4} \quad \text{(M4)}. \tag{12}$$

As shown in Table 1, which compares the boundary-layer properties predicted by P3, P4, and M4 to those ascribed to Blasius [2], one can confirm that, with an error that does not exceed 1.7% over the entire $0 \le y \le \delta$ interval in any of the fundamental properties, M4 outperforms its polynomial counterparts in approximating the traditional Blasius estimates. These include both displacement and momentum thicknesses ($\delta^*$, $\theta$), shape factor $H$, disturbance thickness $\delta$, and skin friction coefficient $C_f$. In contrast, the P3 and P4 profiles lead to appreciably larger peak errors of 9% and 17%, respectively. In fact, by comparing P3 and P4 estimates, it may be seen that P3 outperforms P4 in predicting the non-dimensional displacement and momentum thicknesses, whose errors increase from 9.0% and 4.7% to 13% and 12%, respectively, when P3 is replaced by P4. Moreover, the overall $L_2$ error, which is defined relative to the Blasius solution, increases from 0.034 to 0.054 when Pohlhausen's cubic polynomial is superseded by its quartic form. Here too, the overall $L_2 \approx 0.008$ error that accompanies M4 proves to be lower by one full order of magnitude.

**Table 1. Characteristic boundary-layer predictions and corresponding errors relative to the Blasius solution using three piecewise-analytic velocity profiles [6–8]**

| Profile | $F\left(\dfrac{y}{\delta}\right) \equiv \dfrac{u}{U}$ | $\dfrac{\delta^*}{\delta}$ | $\dfrac{\theta}{\delta}$ | $H = \dfrac{\delta^*}{\theta}$ | $\dfrac{\delta}{x}\sqrt{Re_x}$ | $C_f\sqrt{Re_x}$ | $\dfrac{\delta^*}{x}\sqrt{Re_x}$ | $L_2$ error |
|---|---|---|---|---|---|---|---|---|
| P3 | $\dfrac{3}{2}\dfrac{y}{\delta} - \dfrac{1}{2}\dfrac{y^3}{\delta^3}$ | 0.375 | 0.139 | 2.692 | 4.641 | 0.646 | 1.740 | 0.034 |
| Error | | 9.0% | 4.7% | 4.0% | 7.2% | 2.6% | 1.1% | |
| P4 | $2\dfrac{y}{\delta} - 2\dfrac{y^3}{\delta^3} + \dfrac{y^4}{\delta^4}$ | 0.300 | 0.118 | 2.554 | 5.836 | 0.685 | 1.751 | 0.054 |
| Error | | 13% | 12% | 1.4% | 17% | 3.2% | 1.8% | |
| M4 | $\dfrac{5}{3}\dfrac{y}{\delta} - \dfrac{y^3}{\delta^3} + \dfrac{1}{3}\dfrac{y^4}{\delta^4}$ | 0.350 | 0.134 | 2.618 | 4.993 | 0.668 | 1.748 | 0.008 |
| Error | | 1.7% | 0.52% | 1.1% | 0.13% | 0.53% | 1.6% | |
| Blasius [2] | Eq. (5) [1908 numerics] | 0.344 | 0.133 | 2.59 | 5.000† | 0.664 | 1.72 | |

† Although the 1908 value of 5.0 is still widely used, a more precise modern computation yields 4.9099895 [17].

Upon further scrutiny, what causes Pohlhausen's fourth-order polynomial P4 to deteriorate in predictive capability relative to P3 or M4, despite its ability to secure five boundary conditions instead of four, can be attributed to its incorporation of an overly constraining physical requirement [17]. In the interest of clarity, it may be instructive to revisit the five constraints that each of Pohlhausen's polynomials seeks to satisfy progressively with each successive order. These encompass the velocity adherence condition both at the wall and boundary-layer edge, the vanishing of the shear stress at the edge of the viscous layer, the axial momentum balance at the wall, and, lastly, the vanishing of the normal gradient of the shear stress at the edge of the viscous layer. Mathematically, these physical requirements translate into:

$$u(x,0) = 0 \qquad \text{or} \qquad F(0) = 0 \qquad \text{(inner wall velocity adherence)}, \tag{13}$$

$$u(x,\delta) = U(x) \qquad \text{or} \qquad F(1) = 1 \qquad \text{(outer edge velocity adherence)}, \tag{14}$$

$$\left.\frac{\partial u}{\partial y}\right|_{y=\delta} = 0 \qquad \text{or} \qquad F'(1) = 0 \qquad \text{(negligible outer edge shear stress)}, \tag{15}$$

$$\left.\frac{\partial^2 u}{\partial y^2}\right|_{y=0} = \frac{1}{\mu}\frac{\mathrm{d}p}{\mathrm{d}x} = -\frac{U}{\nu}\frac{\mathrm{d}U}{\mathrm{d}x} \qquad \text{or} \qquad F''(0) = -\Lambda \qquad \text{(pressure-determined wall shear-stress gradient)}, \tag{16}$$

$$\left.\frac{\partial^2 u}{\partial y^2}\right|_{y=\delta} = 0 \qquad \text{or} \qquad F''(1) = 0 \qquad \text{(outer edge shear-stress gradient)}, \tag{17}$$

where Pohlhausen's pressure parameter, which represents a non-dimensional pressure gradient, is given by

$$\Lambda \equiv -\frac{\delta^2}{\mu U}\frac{\mathrm{d}p}{\mathrm{d}x} = \frac{\delta^2}{\nu}\frac{\mathrm{d}U}{\mathrm{d}x} \qquad \text{(Pohlhausen's pressure parameter)}. \tag{18}$$

Note that the fourth condition, Eq. (16), ensures that the axial momentum balance is observed at the wall, wherein the pressure gradient may be exchanged with the farfield velocity gradient by way of Euler's equation [9]. However, as shown in previous work [17], the fifth constraint in Eq. (17) proves to be rather imprecise at the edge of $\delta$. Despite the negligible shear stress at the edge of the viscous layer, its normal gradient continues to change.

To better understand this elusive inconsistency, it is helpful to compare the behavior of the polynomial approximations under consideration to those of the Blasius solution at the endpoints of the viscous layer. This is accomplished in Table 2 where the normalized velocity function $F = u/U$ and its derivatives with respect to the normalized boundary-layer coordinate $\xi$ are compared to their precisely computed values from the exact Blasius equation. As one can immediately see, the assumption of $F''(1) = 0$ for a flat plate with no pressure gradient deviates from the exact Blasius value of $-0.709$ by one order of magnitude. Moreover, M4 provides the closest estimate for the Blasius connection parameter, slope, or constant, $F'(0) = 1.630$, relative to P3 and P4, which, alternatively, yield

**Table 2. Comparison of the endpoint values of P3, P4, and M4 to the traditional Blasius values. All derivatives are taken with respect to $\xi = y/\delta$**

| Profile | $F(\xi) = u/U$ | $F(0)$ | $F'(0)$ | $F''(0)$ | $F(1)$ | $F'(1)$ | $F''(1)$ |
|---------|----------------|--------|---------|----------|--------|---------|----------|
| P3 | $\frac{3}{2}\xi - \frac{1}{2}\xi^3$ | 0 | 1.500 | 0 | 1.000 | 0 | $-3.000$ |
| P4 | $2\xi - 2\xi^3 + \xi^4$ | 0 | 2.000 | 0 | 1.000 | 0 | 0.000 |
| M4 | $\frac{5}{3}\xi - \xi^3 + \frac{1}{3}\xi^4$ | 0 | 1.667 | 0 | 1.000 | 0 | $-2.000$ |
| Blasius [2] | Eq. (5) | 0 | 1.630 | 0 | 0.990 | 0.0904 | $-0.709$ |

1.5 and 2.0, respectively. Clearly, P4 leads to the largest velocity slope disparity at the wall, which helps to justify its tendency to overshoot the Blasius solution relative to P3 or M4. On the other hand, the improved accuracy associated with M4 may be attributed to its ability to observe Pohlhausen's four essential boundary conditions that are consistent with the Blasius estimates, while judiciously avoiding the fifth requirement that deviates from its Blasius counterpart. Lastly, it may be useful to note that Pohlhausen's simplifying assumption of $u = U$ instead of $u = 0.99U$ [or $F(1) = 1$ instead of 0.99] in Table 2 equally affects all piecewise approximations. Only the Blasius solution returns the defining value of 99%, as one expects at $y = \delta$.

## C. Velocity Profiles for Nonzero Pressure Gradients

The foregoing observations explain, at least in part, why Pohlhausen polynomials of order four and higher, which incorporate the fifth condition [Eq. (17)], tend to deteriorate relative to their lower-order forms. Conversely, those that discount the fifth condition tend to be generally more accurate [17]. Bearing these factors in mind, one may proceed by applying the KP approach to the problem involving a variable $U(x)$ and, therefore, a non-vanishing pressure gradient in the farfield region. Using KP3, KP4, and MX4 in reference to the pressure-sensitive polynomials, one obtains, after some algebra (see Appendix B), the following expressions:

$$F(\xi) = \begin{cases} \frac{3}{2}\xi - \frac{1}{2}\xi^3 + \frac{1}{4}\Lambda\left(\xi - 2\xi^2 + \xi^3\right) & \text{(KP3)}, \\ 2\xi - 2\xi^3 + \xi^4 + \frac{1}{6}\Lambda\left(\xi - 3\xi^2 + 3\xi^3 - \xi^4\right) & \text{(KP4)}, \\ \frac{5}{3}\xi - \xi^3 + \frac{1}{3}\xi^4 + \Lambda\left(\frac{83}{400}\xi - \frac{1}{2}\xi^2 + \frac{151}{400}\xi^3 - \frac{17}{200}\xi^4\right) & \text{(MX4)}. \end{cases} \tag{19}$$

In what follows, the same analysis will be repeated using the three representative profiles, whose solutions for flow over a flat plate with a variable pressure gradient will be collectively conveyed to a cylinder in crossflow.

## D. Momentum-Integral Analysis of a Cylinder in Crossflow

In the presence of a variable pressure gradient, $\Lambda$ proves to be a keystone parameters on which most properties of interest depend. At this point in the analysis, however, the distribution of $\Lambda$ around the cylinder remains unknown. As such, the first essential step becomes that of determining the pressure distribution along the surface of the cylinder. This may be accomplished by combining the definition of $\Lambda$ from Eq. (18) and the farfield velocity distribution, $U(x)$, to retrieve a relation linking the disturbance thickness $\delta$ to the spatial location. One gets

$$\delta^2(\phi) = \frac{\nu\Lambda(\phi)}{\mathrm{d}U/\mathrm{d}x} \qquad \text{and so} \qquad \frac{\delta(\phi)}{D} = \sqrt{\frac{\Lambda(\phi)}{4Re_D\cos\phi}}, \tag{20}$$

where $Re_D \equiv U_\infty D/\nu$. Note that Eq. (20) does not directly depend on the assumed velocity profile $F(\xi)$, but rather on the farfield velocity distribution, $U(x)$, which controls the pressure gradient. Consequently, this relation remains valid for all profiles. Bearing this in mind and using Eq. (8) in conjunction with each of the three velocity profiles in the

American Institute of Aeronautics and Astronautics

nearfield, the momentum thickness $\theta$ can be readily evaluated and written in terms of $\Lambda$ and $\delta$, namely,

$$\frac{\theta}{\delta} = \int_0^1 F(1-F)\,\mathrm{d}\xi = \begin{cases} \frac{1}{280}\left(39 - \frac{1}{2}\Lambda - \frac{1}{6}\Lambda^2\right) & \text{(KP3)}, \\[2mm] \frac{1}{63}\left(\frac{37}{5} - \frac{1}{15}\Lambda - \frac{1}{144}\Lambda^2\right) & \text{(KP4)}, \\[2mm] \frac{1}{2520}\left(\frac{3032}{9} - \frac{1159}{300}\Lambda - \frac{29791}{40000}\Lambda^2\right) & \text{(MX4)}. \end{cases} \tag{21}$$

Then, since $\delta(\phi)$ is prescribed by Eq. (20), it may be wholly eliminated from Eq. (21). This enables us to express $\theta$ solely in terms of $\Lambda(\phi)$ and $\phi$, specifically,

$$\frac{\theta(\phi)}{D}\sqrt{Re_D} = \begin{cases} \frac{1}{280}\left(39 - \frac{1}{2}\Lambda - \frac{1}{6}\Lambda^2\right)\sqrt{\dfrac{\Lambda}{4\cos\phi}} & \text{(KP3)}, \\[3mm] \frac{1}{63}\left(\frac{37}{5} - \frac{1}{15}\Lambda - \frac{1}{144}\Lambda^2\right)\sqrt{\dfrac{\Lambda}{4\cos\phi}} & \text{(KP4)}, \\[3mm] \frac{1}{2520}\left(\frac{3032}{9} - \frac{1159}{300}\Lambda - \frac{29791}{40000}\Lambda^2\right)\sqrt{\dfrac{\Lambda}{4\cos\phi}} & \text{(MX4)}. \end{cases} \tag{22}$$

At this juncture, it proves helpful to recall the elegant transformation produced by Walz [15] and fitted to a substantial body of experimental measurements; the resulting formulation is known for providing a straightforward integral relation between the momentum thickness and the farfield solution irrespective of the nearfield velocity profile. Being based on empirical measurements rather than viscous models of the nearfield velocity [8], one may estimate the momentum thickness directly from

$$\theta^2 \approx \frac{0.47\nu}{U^6}\int_0^x U^5\,\mathrm{d}x. \tag{23}$$

Practically, one may replace $U(x)$ by the potential flow velocity distribution and switch the integration variable from $x$ to $\phi$; after minor rearrangements, Eq. (23) returns:

$$\frac{\theta(\phi)}{D}\sqrt{Re_D} = \sqrt{\frac{0.1175}{\sin^6\phi}\left(\frac{8}{15} - \frac{\cos^5\phi}{5} + \frac{2\cos^3\phi}{3} - \cos\phi\right)}. \tag{24}$$

Being solely dependent on $\phi$ and generally applicable to any assumed velocity in the boundary-layer region, Eq. (24) provides the closure relation needed to solve this problem. One may proceed by equating the right-hand side of Eq. (24) to the respective right-hand side of Eq. (22) for each of the three candidate functions. This enables us to retrieve an expression for $\Lambda$ as a function of $\phi$ (see Appendix C). Lastly, being limited to a laminar regime, it may be recognized that the validity of the solutions just obtained will cease beyond the point of separation. For this reason, it is essential to determine the range of $\Lambda$ leading up to $\phi = \phi_{\text{sep}}$. The latter can be evaluated at the point where the laminar shear stress at the wall vanishes, i.e., $s \equiv (\partial u/\partial y)|_{y=0} = 0$. More specifically, by suppressing the first derivative of the normalized velocity at the wall (a quantity that we have labeled as "$s$" in previous work [17]), the critical value of $\Lambda$ may be determined. One finds:

$$s(\Lambda) = \begin{cases} \frac{3}{2} + \frac{1}{4}\Lambda_{\text{sep}} = 0 & \text{(KP3)}, \\[2mm] 2 + \frac{1}{6}\Lambda_{\text{sep}} = 0 & \text{(KP4)}, \\[2mm] \frac{5}{3} + \frac{83}{400}\Lambda_{\text{sep}} = 0 & \text{(MX4)}. \end{cases} \tag{25}$$
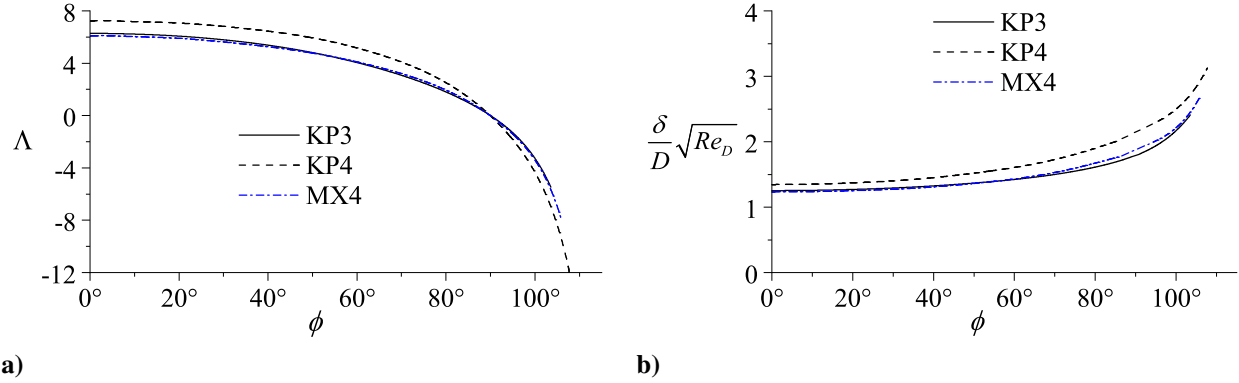
The separation values are thus found to be $\Lambda_{\text{sep}} = -6$ (KP3), $-12$ (KP4), and $-8.0321$ (MX4). As indicated earlier, having a direct correlation of the form $\Lambda = \Lambda(\phi)$ in hand, one may set $\Lambda(\phi_{\text{sep}}) = \Lambda_{\text{sep}}$ and deduce the separation angle for each of the assumed profiles as well as the critical pressure gradient at the point of separation.

For the reader's convenience, the separation angles that accompany these models are evaluated and summarized in Table 3 along with the accrued errors relative to the numerical projection of $\phi_{\text{sep}} = 105°$ reported by Žukauskas and Žiugžda [36]. The latter employs a modification of the finite-difference method of Patankar and Spalding [37] where a partial derivative solution of the linear differential equations of motion is substituted for the original finite-difference approach. Accordingly, the partial differential equations representing continuity and axial momentum are discretized using forward differences and then solved using an explicit marching technique to calculate $u$ and $v$ until $C_f$ is suppressed at the point where $(\partial u/\partial y)|_{y=0} = 0$.

**Table 3.  Separation angle using three different velocity profiles with the corresponding errors relative to numerical prediction of $\phi_{sep} = 105°$ reported by Žukauskas and Žiugžda [36]**

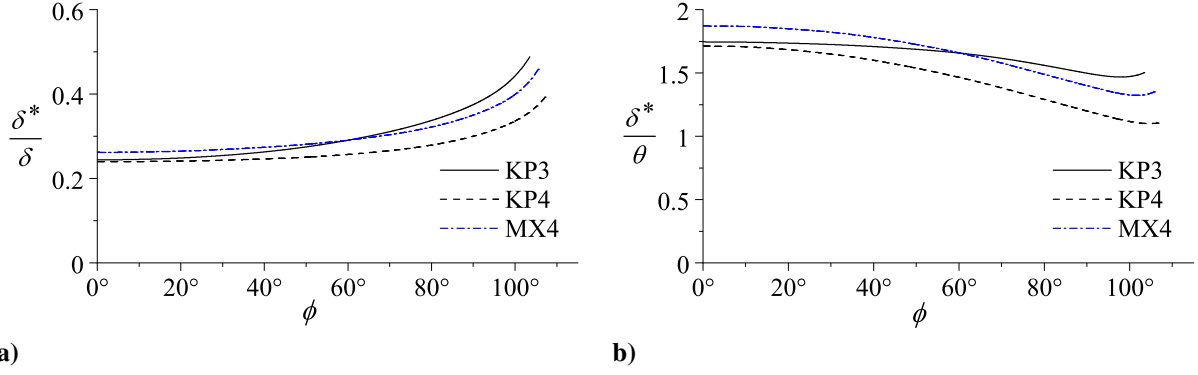| Profile | KP3 | KP4 | MX4 |
|---|---|---|---|
| Separation angle | 103.56° | 107.71° | 105.91° |
| Error | 1.37% | 2.58% | 0.87% |



a)

b)

**Fig. 2.  Profile-dependent angular variations of a) the non-dimensional pressure gradient parameter $\Lambda$ as well as b) the normalized hydrodynamic disturbance thickness $\delta\sqrt{Re_D}/D$.**

Interestingly, the same compact MX4 profile, which has been previously shown to outperform other polynomial approximations at the same order or lower, namely, in predicting boundary-layer characteristics for flow over a flat plate [9], continues to provide the most accurate estimate of the separation point for flow over a cylinder. By exhibiting a mere relative error of 0.87%, the pressure-augmented MX4 profile given by Eq. (19) may be viewed as being practically equivalent to the numerical simulations conducted by Žukauskas and Žiugžda [36]. As for KP3 and KP4, their projections also seem to be fair, although the error entailed in the KP4 model is almost twice that of KP3. Such a perplexing outcome could have been anticipated by recognizing that KP4 is compelled to satisfy a rather imprecise boundary condition in Eq. (17), particularly, which stands at the root of the Pohlhausen paradox [17].

To further complement the tabulated values, the angular distributions of Pohlhausen's pressure parameter $\Lambda(\phi)$ as well as a normalized form of the hydrodynamic disturbance thickness $\delta\sqrt{Re_D}/D$ are provided in Fig. 2 as functions of the azimuthal angle $\phi$. These are supplied for each of the velocity profiles using solid (KP3), broken (KP4), and chained (MX4) lines. Unsurprisingly, these profile-dependent angular variations show strong similarities, especially between MX4 and KP3, which remain the two most accurate models. As for KP4, its disparities are quite visible in both Fig. 2a and Fig. 2b. Based on Part (a), the pressure parameter may be seen to range from $\Lambda_0 = 6.075$ (MX4), 6.274 (KP3), and 7.215 (KP4) at the front stagnation point down to $\Lambda_{sep} = -8.0321$, $-6$, and $-12$, respectively.

Based on Part (b), one confirms that the largest boundary-layer thicknesses in all models are realized at the point of separation and that $\delta$ at the front stagnation point is not zero, but rather finite. Graphically, one may estimate starting values of $\delta\sqrt{Re_D}/D \approx 1.232$ (MX4), 1.252 (KP3), and 1.343 (KP4) at the nose of the cylinder and ending values of 2.681, 2.411, and 3.123, respectively. Subsequently, using the boundary-layer thickness $\delta$, the normalized displacement thickness $\delta^*/\delta$ can be evaluated and displayed, as shown in Fig. 3a. The normalized displacement thickness follows a closely similar increasing trend to that of $\delta$; both are characterized by slow variations between the front stagnation point at $\phi = 0°$ and halfway to separation at approximately $53°$, and these are followed by progressive steepening as the separation point is approached. More specifically, one can see that the initial values of $\delta^*/\delta$ vary, in descending order, from 0.262 (MX4) to 0.244 (KP3), and then 0.240 (KP4). As for the peak displacement values that occur at separation, KP3 is seen to supersede MX4 (starting at around $60°$) to reach a maximum value of 0.488 (KP3), whereas MX4 and KP4 reach 0.464 and 0.398, respectively. Along similar lines, the maximum value of the momentum shape factor $H$ at the front stagnation point in Fig. 3b starts at 1.873 (MX4), 1.746 (KP3), and 1.714 (MX4); it then decreases to a minimum that is reached just before the separation point; the minimum shape factor obtained for each profile is thus found to be 1.468 (KP3), 1.323 (MX4), and 1.099 (KP4). As such, all three profiles predict $\delta^* > \theta$ or

American Institute of Aeronautics and Astronautics

**Fig. 3.  Profile-dependent angular variations of a) the normalized local displacement thickness $\delta^*/\delta$ and b) the dimensionless momentum shape factor $H = \delta^*/\theta$.**

$H > 1$ over the entire physical range, in full conformance to boundary-layer theory. Interestingly, both the normalized displacement thickness and momentum shape factor associated with KP3 start below those of MX4 and then switch order at $\phi \approx 60°$, thus leading to lower values of MX4-based $\delta^*$ and $H$ relative to KP3 at separation. As for KP4, its predictions undershoot those of MX4. As a result, MX4 properties such as $\Lambda$, $\delta$, $\delta^*$, and $H$ in both Figs. 2 and 3 may be seen to serve as the middle ground by falling strictly between their KP3 and KP4 values at separation. This behavior may be attributed to the initial velocity slope of MX4 being bracketed by the slopes of KP3 and KP4, as per Eq. (25).

### E. Viscous Boundary-Layer Characteristics

Having determined the normalized pressure distributions for each model from stagnation to separation, other characteristic properties may be readily evaluated. For example, the local skin friction coefficient $C_f$ may be deduced from the non-dimensional ratio of the wall shear stress and the dynamic pressure. As usual, one can put

$$C_f = \frac{\tau_w}{\frac{1}{2}\rho U_\infty^2} = \frac{\mu\left(\partial u/\partial y\right)|_{y=0}}{\frac{1}{2}\rho U_\infty^2}. \tag{26}$$

By inserting each of the individual velocity profiles into Eq. (26) and rearranging, the local skin friction may be straightforwardly retrieved. One gets:
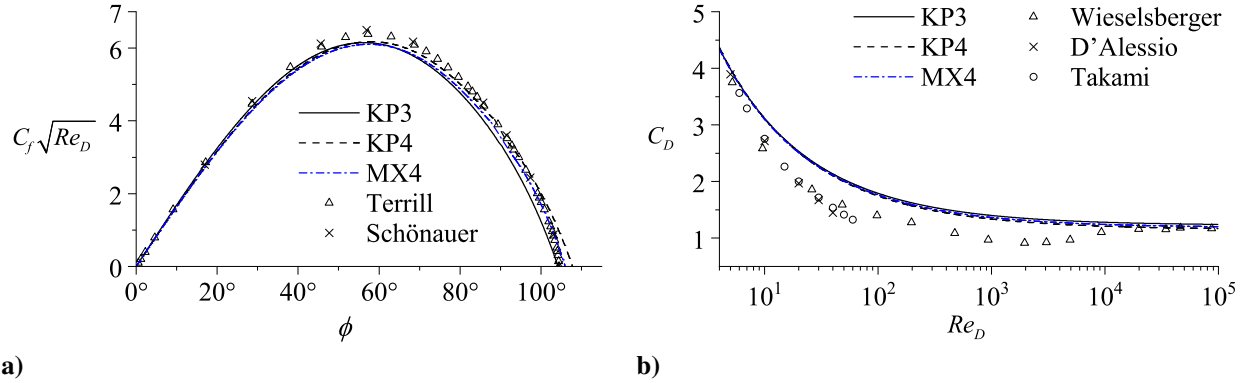
$$C_f\sqrt{Re_D} = \begin{cases} 8\left(\frac{3}{2} + \frac{1}{4}\Lambda\right)\sin\phi\sqrt{\dfrac{\cos\phi}{\Lambda(\phi)}} & \text{(KP3)}, \\[3mm] 8\left(2 + \frac{1}{6}\Lambda\right)\sin\phi\sqrt{\dfrac{\cos\phi}{\Lambda(\phi)}} & \text{(KP4)}, \\[3mm] 8\left(\frac{5}{3} + \frac{83}{400}\Lambda\right)\sin\phi\sqrt{\dfrac{\cos\phi}{\Lambda(\phi)}} & \text{(MX4)}. \end{cases} \tag{27}$$

It may be instructive to note that, as one may have anticipated, the first-order derivative or slope of the velocity profile at the wall, which is given by Eq. (25), appears in the local skin friction coefficient rather explicitly, as it does in several other flow properties. This reaffirms the influential role that the slope plays in controlling the momentum-integral solution. Furthermore, since Eq. (27) is solely dependent on $\phi$, $C_f$ may be characterized in Fig. 4a as a function of $\phi$ up to the separation point. Therein, the skin friction coefficient associated with each of the models is reproduced and compared to the numerical predictions of Schönauer [38] as well as the series approximation provided by Terrill [39]; the former relies on an implicit finite difference method for treating laminar, incompressible, stationary boundary layers over impermeable cylinders using Crocco's differential equation.

Forthwith, it may be seen that the chained MX4 line stays in fair agreement with the computations performed by both Schönauer [38] and Terrill [39], especially as the separation point is approached in Fig. 4a. The enhanced agreement is portrayed further in Table 4, where MX4 can be ascertained to predict the lowest $L_2$ error of the three profiles under consideration as compared to the aforementioned results of Schönauer [38] and Terrill [39]. Graphically,

American Institute of Aeronautics and Astronautics

**Table 4.** $L_2$ **error for the local skin friction** $C_f\sqrt{Re_D}$ **relative to the numerical results of Schönauer [38] and Terrill [39] using three different velocity profiles**

| Profile | KP3 | KP4 | MX4 |
|---|---|---|---|
| $L_2$ error (Schönauer) | 1.195 | 1.186 | 0.958 |
| $L_2$ error (Terrill) | 1.057 | 1.166 | 0.822 |



a)  b)

**Fig. 4. Profile-dependent variations of a) the normalized local skin friction coefficient** $C_f\sqrt{Re_D}$ **as a function of** $\phi$ **relative to numerical predictions by both Schönauer [38] and Terrill [39]. Also shown is b) the total drag coefficient** $C_D$ **as a function of** $Re_D$ **relative to experimental measurements by Wieselsberger [40] side-by-side with numerical simulations by Takami [41] as well as D'Alessio and Dennis [42].**

one may also identify that the maximum skin friction coefficient $(C_f)_{\max}$ takes on the values of 6.1063 (MX4), 6.1500 (KP3), and 6.1758 (KP4) at the particular angles of $\phi_{\max} = 57.53°$, $56.23°$, and $58.04°$, respectively. Here too, the momentum-integral predictions seem to agree rather well with Schönauer's computations, which yield a $(C_f)_{\max} \approx 6.494$ at $\phi_{\max} \approx 56.95°$, as well as Terrill's predictions of $(C_f)_{\max} \approx 6.383$ at $\phi_{\max} \approx 57.3°$. In comparison to Schönauer's and Terrill's, the MX4 overpredicts the locus of $(C_f)_{\max}$ by only 1.02% and 0.40%, respectively.

At this juncture, having fully determined the local $C_f$ behavior, one may proceed to calculate the total friction exerted over the cylinder; this can be achieved by integrating the local skin friction coefficient over the attached segment of the cylinder. The resulting friction drag coefficient may be calculated from [9]:

$$C_{D_f} = \int_0^{\phi_{\text{sep}}} C_f \sin\phi \, \mathrm{d}\phi. \tag{28}$$

In the above, we note that the integration bounds on $\phi$ do not cover the entire back of the cylinder. Instead, they range from zero at stagnation to $\phi_{\text{sep}}$ at separation. Recognizing that $C_f$ suddenly drops to zero when the flow detaches, one does not expect an appreciable contribution of the shear stress over the rear portion of the cylinder. Solving Eq. (28) for the respective profiles and rearranging, one obtains:

$$C_{D_f}\sqrt{Re_D} = \begin{cases} 5.5230 & \text{(KP3)}, \\ 5.7963 & \text{(KP4)}, \\ 5.6259 & \text{(MX4)}. \end{cases} \tag{29}$$

Another figure of merit consists of the pressure or form drag coefficient; this property takes into account the existence of a higher pressure along the front portion of the cylinder as opposed to the lower pressure forming along its rear portion. The normalized pressure difference and, in turn, the non-dimensional local pressure coefficient, may be evaluated from

$$C_P = \frac{\Delta p}{\frac{1}{2}\rho U_\infty^2} = 2\left(1 - \cos 2\phi\right) + \frac{8}{Re_D}\left(1 - \cos\phi\right). \tag{30}$$

11

Since the relations used to derive Eq. (30) depend solely on the farfield velocity, the resulting expression for $C_P$ remains valid for any assumed profile. As with the local skin friction and associated drag coefficients, the pressure drag $C_{D_p}$ can be determined by integrating $C_P$ over the entire area of interest. As before, the bounds of integration start from the frontal stagnation point and extend all the way to separation. Algebraically, one computes

$$C_{D_p} = \int_0^{\phi_{\text{sep}}} C_P \cos\phi \, \mathrm{d}\phi. \tag{31}$$

At first glance, Eq. (31) may appear to be invariant with respect to the assumed velocity profile; however, since each profile leads to a different separation point, dissimilarities in the pressure drag prediction can be expected. One gets

$$C_{Dp} = \begin{cases} 1.2249 + \dfrac{1.4587}{Re_D} & \text{(KP3)}, \\[2mm] 1.1526 + \dfrac{1.2604}{Re_D} & \text{(KP4)}, \\[2mm] 1.1860 + \dfrac{1.3546}{Re_D} & \text{(MX4)}. \end{cases} \tag{32}$$

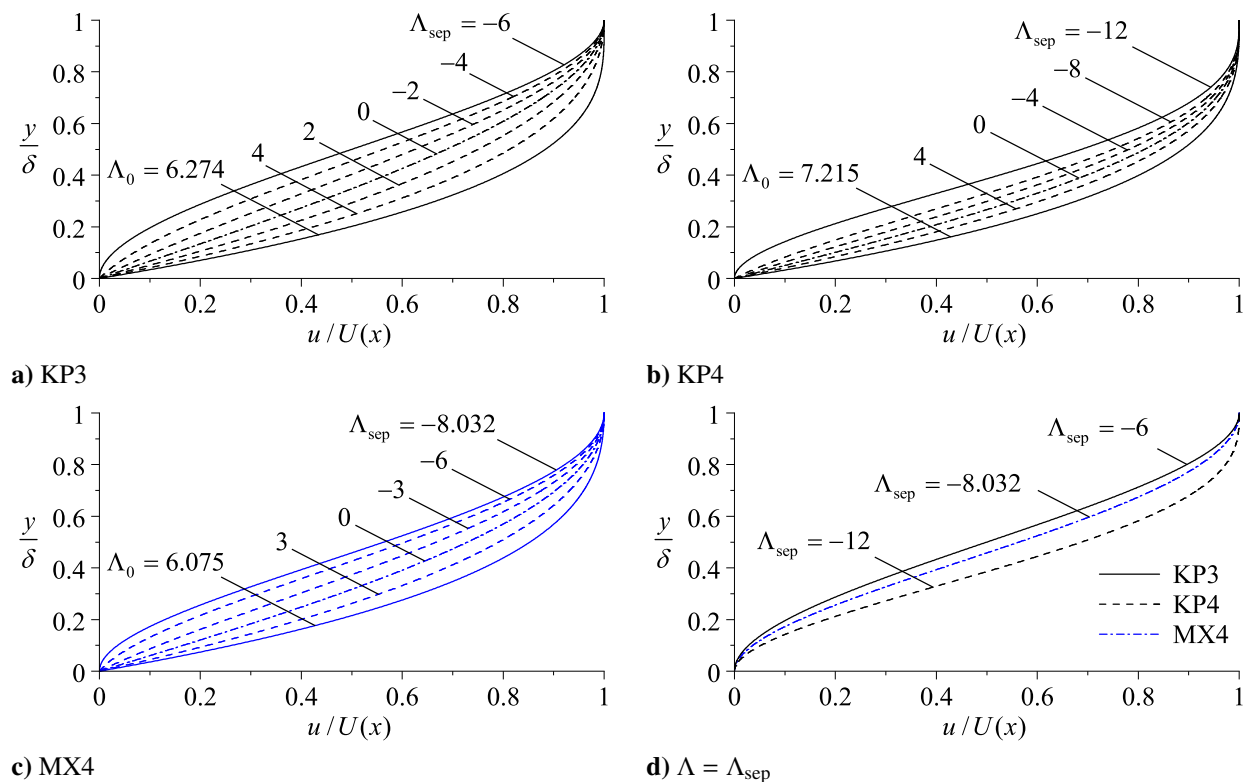Now that both $C_{D_f}$ and $C_{Dp}$ are in hand, the total drag coefficient may be deduced. One obtains

$$C_D = C_{Df} + C_{Dp} = \begin{cases} 1.2249 + \dfrac{1.4587}{Re_D} + \dfrac{5.5230}{\sqrt{Re_D}} & \text{(KP3)}, \\[2mm] 1.1526 + \dfrac{1.2604}{Re_D} + \dfrac{5.7963}{\sqrt{Re_D}} & \text{(KP4)}, \\[2mm] 1.1858 + \dfrac{1.3538}{Re_D} + \dfrac{5.6259}{\sqrt{Re_D}} & \text{(MX4)}. \end{cases} \tag{33}$$

Forthwith, the dependence of $C_D$ on the Reynolds number is illustrated in Fig. 4b for each of the guessed functions. This is carried out over a range of $4 < Re_D < 10^5$, where the rapid depreciation of $C_D$ is demonstrated in the fully laminar range from 4.3 at $Re_D = 4$ to a value of 1.3 at $Re_D = 10^3$. Beyond this point, the drag coefficient appears to asymptote very slowly to a value of about 1.2 as transition is approached. Note that the analytical results are accompanied by experimental measurements due to Wieselsberger [40]. The latter are based on wind-tunnel tests conducted on a cylinder in crossflow using air as the working fluid and a wide range of diameters. They are also compared to numerical predictions by Takami [41] as well as D'Alessio and Dennis [42]. In these works, Takami [41] relies on an iterative finite-difference technique to tackle the cylinder in crossflow over a range of Reynolds numbers whereas D'Alessio and Dennis [42] decompose the solution domain into an inner region where boundary-layer characteristics are resolved and an outer region where wake flow phenomena are modeled.

## F. Topology of the Wall-Tangential and Wall-Normal Velocity Profiles

Lastly, with $u = UF$ in hand, one may use continuity to deduce the normal component of velocity $v$ as shown in detail in Appendix D. One may then proceed to characterize the variation of both $u/U$ and $v/U$ with the pressure parameter or, alternatively, $\phi$. The former is illustrated in Figs. 5a–5c where the non-dimensional component $u/U$ is displayed at several distinct values of $\Lambda$ for each of the three profiles. These range from the peak adverse pressure gradient $\Lambda_{\text{sep}}$ at separation to the largest allowable pressure gradient $\Lambda_0$ at the front stagnation point. In the interest of clarity, all three profiles at separation are gathered and further compared side-by-side in Fig. 5d. Therein, one may note the vertically tangential slope at $y = 0$, which clearly reflects the vanishing shear stress requirement at the wall, $(\partial u/\partial y)|_{y=0} = 0$. One may also infer that the shear stress associated with the MX4 profile continues to serve as a compromise between its KP3 and KP4 values, which either undershoot or overshoot the local shear stress, respectively.

As for the behavior of the normal velocity $v\sqrt{Re_D}/U_\infty$, which is formulated in Appendix D, it is displayed in Figs. 6a–6c at several equispaced angles taken in 20° increments around the cylinder and ranging from the stagnation point at $\phi = 0°$ to the back of the cylinder, where $\phi = 100°$. For the sake of completeness, the normal velocity profiles at their separation angles are collected and displayed side-by-side in Fig. 6d. Interestingly, the change in $v$ from the wall to the edge of the boundary layer broadens as one moves further away from the front stagnation point toward separation, thus illustrating the gradual increase in $v_{\max}$ around the cylinder. Graphically, it can be seen that the normal

12

American Institute of Aeronautics and Astronautics

**a)** KP3



**b)** KP4
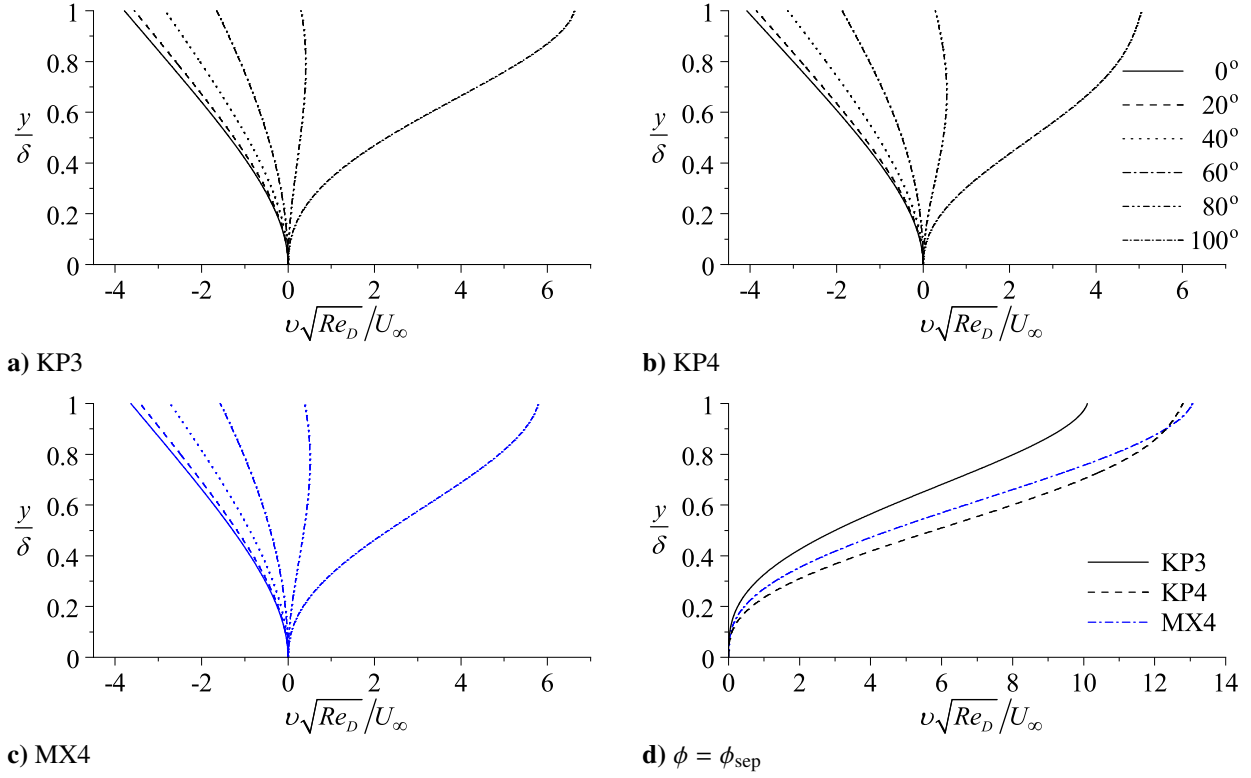


**c)** MX4



**d)** $\Lambda = \Lambda_{\text{sep}}$

**Fig. 5. Spatial variation of the non-dimensional tangential velocity $u/U$ at several distinct values of $\Lambda$ that range from stagnation to separation according to a) KP3, b) KP4, and c) MX4. Part d) provides a comparison of all three profiles at separation.**

velocity, which occurs at the separation point, attains a maximum value of $v_{\text{max}} = 13.060$ (MX4), 12.798 (KP4), and 10.108 (KP3), in descending order. Interestingly, despite KP4 predicting higher values of $v$ over the vast majority of the boundary-layer thickness, it is exceeded by MX4 near the edge of the boundary layer, specifically, in the top 10% of $\delta$. As a result, MX4 may be seen to predict the highest $v_{\text{max}}$ of the three profiles at separation, with KP3 providing the most conservative values of $v$ everywhere.
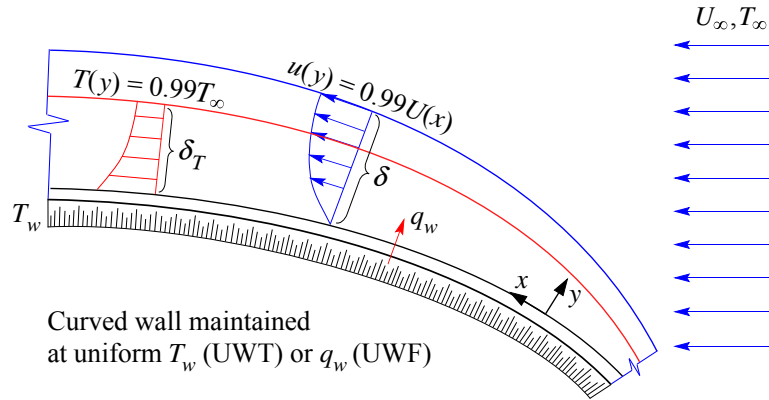
## III. Thermal Analysis

### A. Thermal Configurations and Temperature Profiles

Having showcased the effectiveness of the momentum-integral approach, when used in conjunction with rationally-optimized polynomial approximations, at predicting viscous boundary-layer characteristics, one may invoke the Reynolds analogy to extend this procedure to the heat transfer analysis of thermal boundary layers, specifically, for flow past a cylinder. The latter can be achieved by coupling the momentum-integral formulation with the energy balance equation given by Eq. (4). The main objective of the thermal analysis will be to model the thermal layer in the process of determining a Nusselt number correlation that is suitable for predicting convective heat transfer from the surface of the cylinder. To do so, two canonical thermal configurations will be considered, as depicted schematically in Fig. 7. In the first, isothermal case, the surface of the cylinder will be maintained at a uniform wall temperature (UWT); in the second, isoflux case, the cylinder will be subjected to a uniform wall flux (UWF). In both situations, the temperature of the wall $T_w$ will be taken to exceed $T_\infty$, thus leading to two cases of freestream heating. Accordingly, $T_w$ will remain spatially invariant in the UWT configuration and, conversely, the wall heat flux per unit area $q_w$ will be held constant in the UWF configuration. As usual, the edge of the thermal boundary layer will be situated at $y = \delta_T$, where $\delta_T$ denotes the thermal layer thickness [9]. At such a distance, the temperature would have practically reached its freestream value and the normal gradients of the temperature in the $y$-direction would have nearly vanished. Using

**a)** KP3        **b)** KP4

**c)** MX4        **d)** $\phi = \phi_{\text{sep}}$

**Fig. 6. Spatial variation of the non-dimensional normal velocity $v\sqrt{Re_D}/U_\infty$ at several distinct values of $\phi$ that range from stagnation to near separation according to a) KP3, b) KP4, and c) MX4. Part d) provides a comparison of all three profiles at separation.**



**Fig. 7. Schematics of the viscous and thermal boundary layers, $\delta$ and $\delta_T$, for the two fluid heating scenarios corresponding to either a curved surface at uniform wall temperature (UWT) or heat flux (UWF).**

$k_f$ to designate the fluid's thermal conductivity, the boundary conditions for the ensuing two-pronged problem can be expressed as

$$y = 0; \qquad \begin{cases} T = T_w & \text{(uniform wall temperature, UWT case),} \\ \dfrac{\partial T}{\partial y} = -\dfrac{q_w}{k_f} & \text{(uniform wall flux, UWF case),} \end{cases} \qquad (34a)$$

14

American Institute of Aeronautics and Astronautics

and, for both cases,

$$y = \delta_T; \quad T = T_\infty \quad \text{with} \quad \frac{\partial T}{\partial y} = 0. \tag{34b}$$

Based on the Reynolds analogy and the technique used recently by Majdalani and Xuan [17], a total of six thermal profiles may be defined, particularly, two for each of the KP3, KP4, and MX4 models depending on whether isothermal or isoflux requirements are imposed. In summary, one may define $\xi_T \equiv y/\delta_T$ and obtain, under isothermal conditions, the following reduced temperature distributions:

$$\frac{T - T_\infty}{T_w - T_\infty} = \begin{cases} 1 - \frac{3}{2}\xi_T + \frac{1}{2}\xi_T^3 & \text{(KP3, UWT)}, \\ 1 - 2\xi_T + 2\xi_T^3 - \xi_T^4 & \text{(KP4, UWT)}, \\ 1 - \frac{5}{3}\xi_T + \xi_T^3 - \frac{1}{3}\xi_T^4 & \text{(MX4, UWT)}. \end{cases} \tag{35}$$

Similarly, under isoflux conditions, one recovers:

$$\frac{T - T_\infty}{q_w \delta_T / k_f} = \begin{cases} \frac{2}{3}\left(1 - \frac{3}{2}\xi_T + \frac{1}{2}\xi_T^3\right) & \text{(KP3, UWF)}, \\ \frac{1}{2}\left(1 - 2\xi_T + 2\xi_T^3 - \xi_T^4\right) & \text{(KP4, UWF)}, \\ \frac{3}{5}\left(1 - \frac{5}{3}\xi_T + \xi_T^3 - \frac{1}{3}\xi_T^4\right) & \text{(MX4, UWF)}. \end{cases} \tag{36}$$

In the interest of clarity, Eqs. (35) and (36) are illustrated side-by-side in Fig. 8. Graphically, one may readily infer that the MX4-based temperature profile (chained line) remains bracketed, for both UWT and UWF configurations, by the KP3 (solid) and KP4 (broken) lines, which slightly overshoot and undershoot its value at any vertical distance from the wall, respectively. Although these thermal distributions are based on the Reynolds analogy for flow over a flat plate, the small size of $\delta_T$ in comparison to the curvature of a typical cylinder in crossflow may be used to justify the present extension [9].
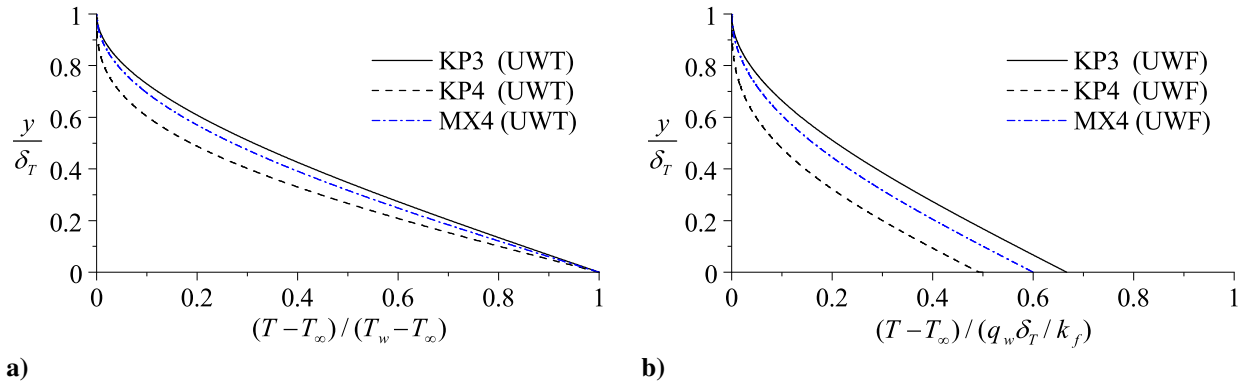
## B. Isothermal Momentum-Integral Analysis

As shown in Appendix E, the integro-differential form of the energy balance relation for the isothermal case can be expressed as:

$$\frac{\partial}{\partial x} \int_0^{\delta_T} (T - T_\infty) u \, dy = -\alpha \left. \frac{\partial T}{\partial y} \right|_{y=0}, \tag{37}$$

where, as before, $\alpha$ represents the thermal diffusivity. By substituting the velocity profiles from Eq. (19) as well as the temperature profiles from Eq. (35) into Eq. (37), one retrieves, after some simplifications:

$$\delta_T \frac{\partial}{\partial x} \left[ U(x)\delta_T \zeta \left(\frac{3}{2} + \frac{1}{4}\Lambda\right) \right] = 15\alpha \qquad \text{(KP3)}, \tag{38}$$



**Fig. 8. Profile-dependent spatial variation of the reduced temperature distribution within the thermal boundary layer for a) UWT and b) UWF thermal configurations.**

15

American Institute of Aeronautics and Astronautics

$$\delta_T \frac{\partial}{\partial x} \left[ U(x)\delta_T \zeta \left( 2 + \tfrac{1}{6}\Lambda \right) \right] = 30\alpha \qquad \text{(KP4)}, \tag{39}$$

and

$$\delta_T \frac{\partial}{\partial x} \left[ U(x)\delta_T \zeta \left( \tfrac{5}{3} + \tfrac{83}{400}\Lambda \right) \right] = \frac{75}{4}\alpha \qquad \text{(MX4)}, \tag{40}$$

where $\zeta \equiv \delta_T/\delta$ captures the thermal-to-viscous ratio of boundary-layer thicknesses. In practice, $\zeta < 1$ when the Prandtl number, $Pr$, is found to exceed unity. In fact, Majdalani and Xuan [17] show that $\zeta = Pr^{-1/3} + O(Pr^{-1})$ provides an excellent approximation so long as $Pr > 0.3$; as such, higher-order corrections for $\zeta = Pr^{-1/3}$ may be safely discounted. A similar assumption will be later adopted in the isoflux analysis, since switching to the UWF condition does not alter the order of $\zeta$.

At this juncture, integrating the energy balance expressions of Eqs. (38–40) with respect to $x$ enables us retrieve closed-form relations for the normalized $\delta_T$ as a function of the azimuthal angle $\phi$. After some effort, we obtain

$$\bar{\delta}_T(\phi) \equiv \frac{\delta_T(\phi)}{D} Re_D^{1/2} Pr^{1/3} = \begin{cases} \sqrt[3]{\dfrac{15 \int_0^\phi \left( \tfrac{3}{2} + \tfrac{1}{4}\Lambda \right) \sin\phi \, \mathrm{d}\phi}{4 \left( \tfrac{3}{2} + \tfrac{1}{4}\Lambda \right)^2 \sin^2\phi}} \sqrt{\dfrac{\Lambda}{\cos\phi}} & \text{(KP3)}, \\[6mm] \sqrt[3]{\dfrac{15 \int_0^\phi \left( 2 + \tfrac{1}{6}\Lambda \right) \sin\phi \, \mathrm{d}\phi}{2 \left( 2 + \tfrac{1}{6}\Lambda \right)^2 \sin^2\phi}} \sqrt{\dfrac{\Lambda}{\cos\phi}} & \text{(KP4)}, \\[6mm] \sqrt[3]{\dfrac{75 \int_0^\phi \left( \tfrac{5}{3} + \tfrac{83}{400}\Lambda \right) \sin\phi \, \mathrm{d}\phi}{16 \left( \tfrac{5}{3} + \tfrac{83}{400}\Lambda \right)^2 \sin^2\phi}} \sqrt{\dfrac{\Lambda}{\cos\phi}} & \text{(MX4)}, \end{cases} \tag{41}$$

where $\bar{\delta}_T(\phi)$ denotes the normalized group parameter that combines the thermal boundary-layer thickness with $D$, $Re_D$, and $Pr$. Moreover, in terms of the thermal conductivity of the surrounding fluid $k_f$, the local heat transfer coefficient can be written as [35]:

$$h(\phi) = -\frac{k_f}{T_w - T_\infty} \left. \frac{\partial T}{\partial y} \right|_{y=0} = -\frac{k_f}{\delta_T(\phi)} \left. \frac{\mathrm{d}\left[ (T - T_\infty)/(T_w - T_\infty) \right]}{\mathrm{d}\xi_T} \right|_{\xi_T=0}. \tag{42}$$

After substituting the modeled temperature distributions from Eq. (35) into Eq. (42), the profile-specific local heat transfer coefficient can be determined using:

$$h(\phi)\delta_T(\phi) = \begin{cases} \tfrac{3}{2}k_f & \text{(KP3)}, \\ 2k_f & \text{(KP4)}, \\ \tfrac{5}{3}k_f & \text{(MX4)}. \end{cases} \tag{43}$$

At this point, rearranging Eq. (41) and substituting it into Eq. (43) enables us to construct the local Nusselt number correlation for each of the three thermal profiles. We get

$$\left. \frac{Nu_D(\phi)|_{\text{isothermal}}}{Re_D^{1/2} Pr^{1/3}} \right. = \begin{cases} \dfrac{3}{2} \sqrt[3]{\dfrac{4 \left( \tfrac{3}{2} + \tfrac{1}{4}\Lambda \right)^2 \sin^2\phi}{15 \int_0^\phi \left( \tfrac{3}{2} + \tfrac{1}{4}\Lambda \right) \sin\phi \, \mathrm{d}\phi}} \sqrt{\dfrac{\cos\phi}{\Lambda}} & \text{(KP3)}, \\[6mm] 2 \sqrt[3]{\dfrac{2 \left( 2 + \tfrac{1}{6}\Lambda \right)^2 \sin^2\phi}{15 \int_0^\phi \left( 2 + \tfrac{1}{6}\Lambda \right) \sin\phi \, \mathrm{d}\phi}} \sqrt{\dfrac{\cos\phi}{\Lambda}} & \text{(KP4)}, \\[6mm] \dfrac{5}{3} \sqrt[3]{\dfrac{16 \left( \tfrac{5}{3} + \tfrac{83}{400}\Lambda \right)^2 \sin^2\phi}{75 \int_0^\phi \left( \tfrac{5}{3} + \tfrac{83}{400}\Lambda \right) \sin\phi \, \mathrm{d}\phi}} \sqrt{\dfrac{\cos\phi}{\Lambda}} & \text{(MX4)}, \end{cases} \tag{44}$$

where $Nu_D \equiv hD/k_f$ represents the diameter-based Nusselt number.

16

American Institute of Aeronautics and Astronautics

## C. Isoflux Momentum-Integral Analysis

In similar manner, the energy balance statement for the isoflux case can be used to write

$$\frac{\partial}{\partial x} \int_0^{\delta_T} (T - T_\infty) \, u \, \mathrm{d}y = \frac{q_w}{\rho c_p}, \tag{45}$$

where $\rho$ and $c_p$ refer to the density and constant pressure specific heat of the working fluid. To make further headway, the fluid's physical properties can be taken to be constant, an assumption that is often made in the treatment of incompressible laminar flow with no internal heat generation. This enables us to further simplify Eq. (45) into:

$$\frac{\partial}{\partial x} \left[ U(x)\delta_T^2 \zeta \left( \tfrac{3}{2} + \tfrac{1}{4}\Lambda \right) \right] = 15 \frac{\nu}{Pr} \qquad \text{(KP3)}, \tag{46}$$

$$\frac{\partial}{\partial x} \left[ U(x)\delta_T^2 \zeta \left( 2 + \tfrac{1}{6}\Lambda \right) \right] = 30 \frac{\nu}{Pr} \qquad \text{(KP4)}, \tag{47}$$
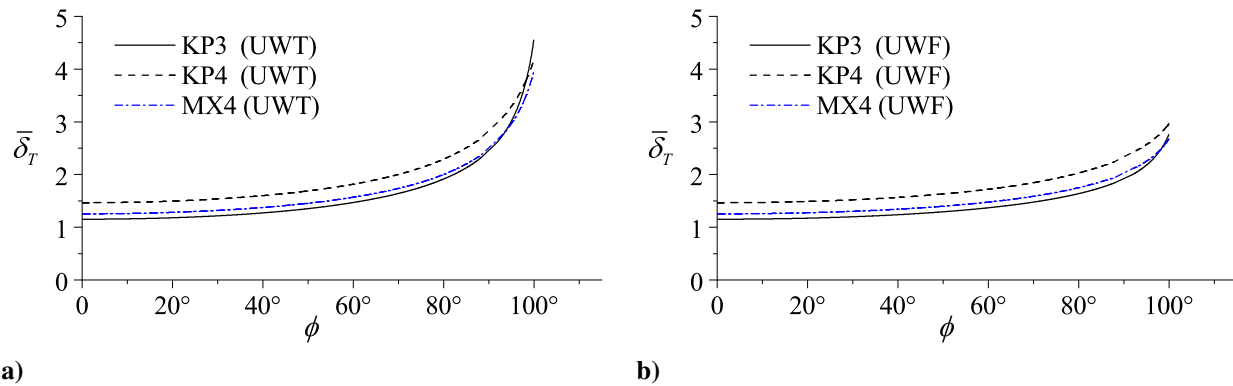
and

$$\frac{\partial}{\partial x} \left[ U(x)\delta_T^2 \zeta \left( \tfrac{5}{3} + \tfrac{83}{400}\Lambda \right) \right] = \frac{75}{4} \frac{\nu}{Pr} \qquad \text{(MX4)}. \tag{48}$$

Lastly, one may integrate Eqs. (46–48) with respect to $x$; the resulting expressions may be readily rearranged, normalized, and simplified into the following relations for the local $\delta_T$:

$$\bar{\delta}_T(\phi) = \frac{\delta_T(\phi)}{D} Re_D^{1/2} Pr^{1/3} = \begin{cases} \sqrt[3]{\dfrac{15\phi}{8\left(\tfrac{3}{2} + \tfrac{1}{4}\Lambda\right)\sin\phi} \sqrt{\dfrac{\Lambda}{\cos\phi}}} & \text{(KP3)}, \\[3ex] \sqrt[3]{\dfrac{15\phi}{4\left(2 + \tfrac{1}{6}\Lambda\right)\sin\phi} \sqrt{\dfrac{\Lambda}{\cos\phi}}} & \text{(KP4)}, \\[3ex] \sqrt[3]{\dfrac{75\phi}{32\left(\tfrac{5}{3} + \tfrac{83}{400}\Lambda\right)\sin\phi} \sqrt{\dfrac{\Lambda}{\cos\phi}}} & \text{(MX4)}. \end{cases} \tag{49}$$

For the reader's convenience, Eqs. (41) and (49) are displayed side-by-side in Fig. 9a for the isothermal and isoflux models. As usual, the MX4-based thermal boundary layer (chained line) remains bounded between the KP3 (solid) and KP4 (broken) lines except at the back of the cylinder, prior to separation, specifically for $\phi \geq 93.5°$ and $98.2°$ for the UWT and UWF configurations, respectively. Everywhere else, the MX4-based $\bar{\delta}_T$ remains closest to the KP3 model approximation, which slightly underestimates its local values.



**Fig. 9. Profile-dependent angular variations of $\bar{\delta}_T \equiv (\delta_T/D)Re_D^{1/2}Pr^{1/3}$ for the two thermal configurations: a) UWT's Eq. (41) and b) UWF's Eq. (49).**

At this stage, having fully characterized the thermal boundary layer, the local heat transfer coefficient may be evaluated and written in terms of the wall heat flux using Newton's law for cooling. One can put
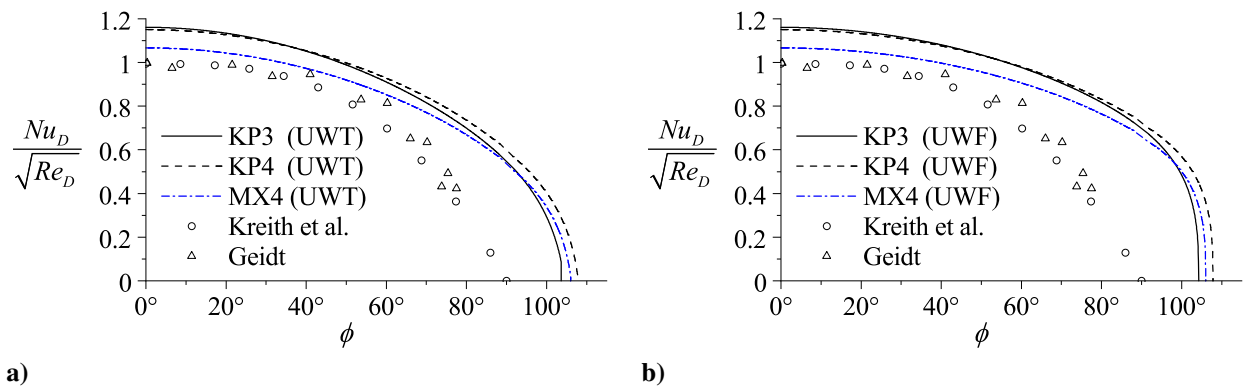
$$h\left(\phi\right) = \frac{q_w}{T\left(\phi\right) - T_\infty}. \tag{50}$$

Then, by consolidating Eq. (49) with Eq. (50), a local Nusselt number correlation may be constructed under isoflux conditions. One gets

$$\frac{Nu_D(\phi)|_{\text{isoflux}}}{Re_D^{1/2}Pr^{1/3}} = \begin{cases} \dfrac{3}{2}\sqrt[3]{\dfrac{4\left(\frac{3}{2} + \frac{1}{4}\Lambda\right)\sin\phi}{15\phi}}\sqrt{\dfrac{\cos\phi}{\Lambda}} & \text{(KP3)}, \\[3ex] 2\sqrt[3]{\dfrac{8\left(2 + \frac{1}{6}\Lambda\right)\sin\phi}{15\phi}}\sqrt{\dfrac{\cos\phi}{\Lambda}} & \text{(KP4)}, \\[3ex] \dfrac{5}{3}\sqrt[3]{\dfrac{32\left(\frac{5}{3} + \frac{83}{400}\Lambda\right)\sin\phi}{75\phi}}\sqrt{\dfrac{\cos\phi}{\Lambda}} & \text{(MX4)}. \end{cases} \tag{51}$$

Using air with $Pr \approx 0.71$, both UWT and UWF cases of Nusselt number correlations, given by Eqs. (44) and (51), are illustrated as a function of $\phi$ in Figs. 10a and 10b using the three analytical models in hand. They are also compared to empirical data reported by Kreith et al. [35] and Giedt [43]. We recall that the empirical relations obtained heretofore are formulated by consolidating the equations of motion and energy as well as tabulated constants based on experimental measurements. Graphically, one may infer that although all formulations follow the same monotonically decreasing trend in $Nu_D/\sqrt{Re_D}$, the closest curves to the empirically acquired values correspond to the MX4 model. This is followed by the KP3 and KP4 formulations, with the latter exhibiting the largest deviations over the physical range of $\phi$. In fact, under both UWT and UWF conditions, the MX4-based thermal formulation predicts the most conservative values of the Nusselt number throughout the vast majority of the angular range relative to its KP3 and KP4 counterparts. The underlying behavior leads to a closer overall agreement with empirical measurements [35, 43] which translates, in turn, into a lower $L_2$ error. This is readily shown in Table 5 where the $L_2$ error based on each of the three analytical models is evaluated and compared to the data by Kreith et al. [35] under both isothermal and isoflux conditions. For the resulting 6 cases, one finds 1.324 (KP3), 1.681 (KP4), and 1.183 (MX4) under UWT conditions, and 1.658 (KP3), 1.959 (KP4), and 1.471 (MX4) under UWF conditions.

As one may have been anticipated, the MX4 model is accompanied by the lowest overall error, particularly, for the UWF case. This is followed by the KP3 and KP4 errors in ascending order; this behavior may be viewed as being consistent with the Pohlhausen paradox observed in flat-plate analysis [17]. Here too, the KP3 model outperforms its higher-order KP4 approximation. Moreover, and for all cases considered, the thermal profiles used in conjunction with the UWT assumption seem to slightly outperform their UWF counterparts. An intriguing yet somewhat foreseeable



a)  b)

Fig. 10.  **Profile-dependent angular variations of the normalized Nusselt number $Nu_D/\sqrt{Re_D}$ as a function of $\phi$ assuming air ($Pr = 0.71$) under both a) isothermal (UWT) and b) isoflux (UWF) conditions; also shown are empirical predictions according to Kreith et al. [35] and Giedt [43].**

**Table 5.** $L_2$ errors of the normalized local Nusselt number $Nu_D/\sqrt{Re_D}$ for three different velocity profiles and both isothermal (UWT) and isoflux (UWF) conditions relative to empirical measurements by Kreith et al. [35]

| Profile | KP3 | KP4 | MX4 |
|---|---|---|---|
| UWT $L_2$ error | 1.324 | 1.681 | 1.183 |
| UWF $L_2$ error | 1.658 | 1.959 | 1.471 |

realization in Figs. 10a and 10b corresponds to the steep decrease after $\phi = 90°$; this sharp drop may be attributed to the sudden shift from a favorable to an adverse pressure gradient as the flow crosses the top of the cylinder. The presence of an adverse pressure gradient triggers rapid changes in boundary-layer characteristics that eventually lead to separation. In hindsight, a similarly abrupt transition may be seen to affect the hydrodynamic properties described in Figs. 2, 4 and 6 past the 90° angle.

## IV. Concluding Remarks

The traditional Kármán–Pohlhausen (KP) momentum-integral approach for boundary-layer analysis is widely used but noted for deteriorating at increasing orders of the Pohlhausen polynomial representing the velocity profile in the nearfield[9]. Rather paradoxically, increasing (rather than decreasing) errors are realized when using fourth and higher-order Pohlhausen polynomials, often leading to discrepancies in boundary-layer estimates that are of order 10-20%. To overcome this perplexing deficiency, other methods have been meticulously devised including those mirrored by Walz [15] and Thwaites [16]. However, unlike Kármán–Pohlhausen's technique, these alternative methods compute the momentum thickness with a fair degree of accuracy; however, they provide no information about the topology of the flowfield inside the viscous region. On the centennial anniversary of the 1921 momentum-integral approach, the underlying deficiency is finally explained and resolved using a dedicated study by Majdalani and Xuan [17]. Therein, the root of the disparity is clarified and attributed to an overly constraining second-order derivative of the axial velocity that is prescribed (too early) by Pohlhausen [4] at the outer edge of the boundary layer. By relaxing this condition, a much improved formulation is readily achieved.

In this work, the Kármán–Pohlhausen momentum-integral approach is shown to be highly effective at predicting the viscous and thermal boundary-layer characteristics associated with the frequently cited benchmark problem of a stationary flow over a cylinder. This is especially true when the KP approach is used in concert with a novel polynomial representation of the velocity and, through the use of the Reynolds analogy, the temperature profile in the nearfield. Dubbed MX4 in the foregoing analysis, this profile is shown to outperform its predecessors, specifically Pohlhausen's KP3 and KP4 profiles, which have been widely used throughout the literature. In comparison to the latter, the MX4 profile leads to more accurate predictions of the separation point at the back of the cylinder as well as the point of maximum shear. These special points are evaluated analytically and shown to produce 0.87% and 1.02% relative errors that fall well within the uncertainty associated with typical experimental measurements. The KP-MX4 approach also leads to better predictions of the thermal boundary-layer characteristics and Nusselt number formulations under both uniform wall temperature and heat flux conditions.

In practice, despite the presence of pressure-gradients, the use of MX4 in lieu of KP4 leads to better overall estimates of both skin friction and pressure drag coefficients and, therefore, total drag. Furthermore, although other integral techniques by Walz [15] and Thwaites [16] can predict the skin friction coefficient based on a momentum thickness evaluation, their integral forms are solely dependent on the farfield velocity $U(x)$. As such, they provide no characteristic information that helps to elucidate the nature of the velocity or thermal profiles across the viscous or thermal boundary layers. In fact, their extrapolation of the momentum thickness may be traced back to a reasonable fit to experimental measurements. In contrast, the present approach can be paired with the KP formulation to predict the boundary-layer characteristics all the way from the surface of the cylinder to the farfield. These include accurate reconstructions of the actual velocity and temperature distributions in the nearfield that directly affect the remaining boundary-layer properties. The parameters that accompany higher-order polynomial approximations of the present approach can also be adjusted to accommodate any sets of measurements or numerical simulations of the flow around the cylinder with a variable pressure gradient. Reducing the error further is therefore possible, as shown by Majdalani and Xuan [17]. So long as the deficient curvature condition at the edge of the boundary layer is judiciously avoided, the projections obtained through this technique seem to be virtually equivalent to numerical simulations of the same

problem. For this reason, it is hoped that the Kármán–Pohlhausen momentum-integral approach will continue to be employed in conjunction with rationally-optimized polynomial approximations, such as the MX4 profile, in future investigations involving other canonical problems and both hydrodynamic and thermal analyses.

## Acknowledgments

## Appendices

## A. Alternative Form of the Blasius Equation

The purpose of this section is to reformulate the Blasius equation in terms of $F(\xi) = u/U$ and derivatives of $\xi$, instead of the characteristic function $f(\eta) = \psi/\sqrt{2\nu x U}$ and derivatives of $\eta$, where $\psi$ and $\eta = y\sqrt{U/(2\nu x)}$ represent the Blasius stream function and similarity variable, respectively, and $\xi = y/\delta$ denotes the fractional distance within the boundary layer [2]. This transformation is performed to better reconcile between the velocity profiles used in the Kármán–Pohlhausen momentum-integral approach, which are expressed in terms of $F(\xi)$, and the velocity distribution computed from the Blasius equation through the derivative function $F(\eta) = df/d\eta$. Assuming viscous motion over a flat plate with a zero pressure gradient, the traditional Blasius equation and its boundary conditions can be written as [9]

$$\frac{\mathrm{d}^3 f}{\mathrm{d}\eta^3} + f\frac{\mathrm{d}^2 f}{\mathrm{d}\eta^2} = 0 \quad \text{with} \quad f(0) = \frac{\mathrm{d}f(0)}{\mathrm{d}\eta} = 0, \quad \text{and} \quad \frac{\mathrm{d}f(\infty)}{\mathrm{d}\eta} = 1. \tag{52}$$

To begin, a straightforward differentiation with respect to $\eta$ yields:

$$\frac{\mathrm{d}^4 f}{\mathrm{d}\eta^4} + f\frac{\mathrm{d}^3 f}{\mathrm{d}\eta^3} + \frac{\mathrm{d}f}{\mathrm{d}\eta}\frac{\mathrm{d}^2 f}{\mathrm{d}\eta^2} = 0. \tag{53}$$

Note that the characteristic function $f$ may be expressed in terms of its derivatives by rearranging the Blasius equation into

$$f = -\frac{\mathrm{d}^3 f/\mathrm{d}\eta^3}{\mathrm{d}^2 f/\mathrm{d}\eta^2}. \tag{54}$$

Since $F(\xi)$ can only be written in terms of the derivative of $f(\eta)$, it is beneficial to eliminate $f$ from the second member of Eq. (53) using Eq. (54). After a simple rearrangement, one gets:

$$\frac{\mathrm{d}^4 f}{\mathrm{d}\eta^4}\frac{\mathrm{d}^2 f}{\mathrm{d}\eta^2} + \frac{\mathrm{d}f}{\mathrm{d}\eta}\left(\frac{\mathrm{d}^2 f}{\mathrm{d}\eta^2}\right)^2 + \left(\frac{\mathrm{d}^3 f}{\mathrm{d}\eta^3}\right)^2 = 0. \tag{55}$$

As emphasized by Majdalani and Xuan [17], the two independent parameters $\eta$ and $\xi$ can be connected using

$$\xi = \frac{\sqrt{2}}{a}\eta \quad \text{and} \quad \frac{\mathrm{d}\xi}{\mathrm{d}\eta} = \frac{\sqrt{2}}{a}, \tag{56}$$

where $a = \delta\sqrt{Re_x}/x = 4.9099895 \approx 4.91$ denotes a characteristic constant of the boundary-layer thickness [17]. Then, using primes to denote differentiation with respect to $\xi$, the chain rule may be used to relate the derivatives of $f(\eta)$ and $F(\xi)$. One collects
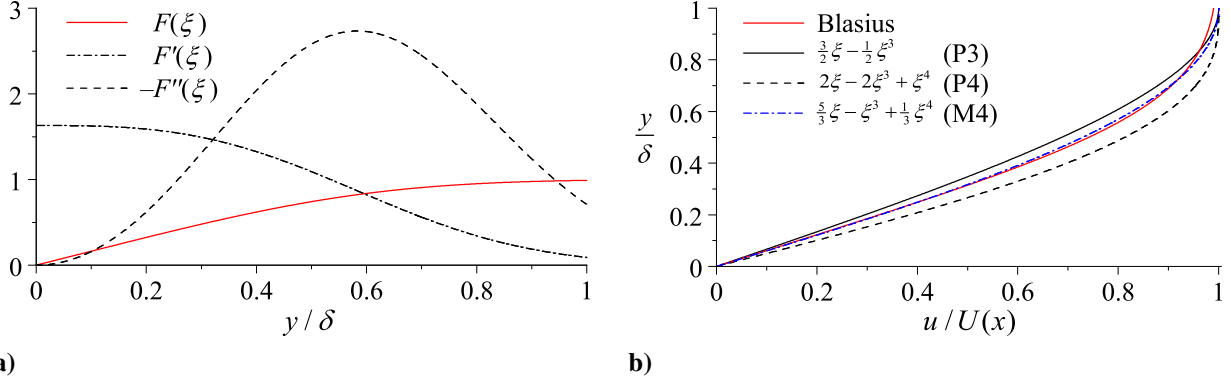
$$\frac{\mathrm{d}^2 f}{\mathrm{d}\eta^2} = \frac{\mathrm{d}F}{\mathrm{d}\eta} = \frac{\mathrm{d}F}{\mathrm{d}\xi}\frac{\mathrm{d}\xi}{\mathrm{d}\eta} = \frac{\sqrt{2}}{a}F'; \quad F' \equiv \frac{\mathrm{d}F}{\mathrm{d}\xi}, \tag{57}$$

$$\frac{\mathrm{d}^3 f}{\mathrm{d}\eta^3} = \frac{2}{a^2}F'', \quad \text{and} \quad \frac{\mathrm{d}^4 f}{\mathrm{d}\eta^4} = \frac{2\sqrt{2}}{a^3}F'''. \tag{58}$$

It can thus be seen that the backward substitution of Eqs. (57) and (58) into Eq. (55) leads to the alternative form,

$$F'''F' - F''^2 + \tfrac{1}{2}a^2 F'^2 F = 0, \quad \text{with} \quad F(0) = F''(0) = 0, \quad \text{and} \quad F(\infty) = 1. \tag{59}$$

American Institute of Aeronautics and Astronautics

**Fig. 11. Numerical solution of a) an equivalent formulation of the Blasius equation given by Eq. (59) directly for the normalized velocity $F(\xi)$ across the boundary-layer region, including its first and second derivatives $F'$ and $F''$. Also shown in Part b) is the normalized Blasius velocity along with its polynomial approximations given by Eqs. (11) and (12) in the absence of a pressure-gradient parameter.**

We thus arrive at another third-order, nonlinear differential equation that is conveniently cast in terms of the normalized velocity function $F(\xi)$. Note that the first and third boundary conditions convey directly from the basic requirements used by Blasius [2] for wall adherence and freestream recovery in the farfield. However, given that $f(0) = 0$ becomes impractical to use, the second condition, $F''(0) = 0$, may be retrieved from Pohlhausen's fourth boundary condition given by Eq. (16). The latter represents the shear-stress gradient at the wall that can be connected to the pressure gradient prescribed by the farfield velocity via Euler's momentum equation. A straightforward numerical solution of the normalized velocity $F$, given by Eq. (59), as well as its first two derivatives, is provided in Fig. 11a. It is also compared in Fig. 11a to its analytical approximations given by the three velocity profiles, P3, P4 and M4, which exclude a pressure-gradient correction. Clearly, M4 displays the closest agreement with the exact Blasius distribution and is followed by P3 and P4, respectively.

## B. Pressure-Sensitive Velocity Profiles

In order to specify the unknown polynomial coefficients that can be used to construct the piecewise analytic velocity profiles across the boundary-layer region, four of Pohlhausen's fundamental boundary conditions given by Eqs. (13–16) may be applied to a generic quartic polynomial of the form

$$F(\xi) = c_0 + s\xi + c_2\xi^2 + c_3\xi^3 + c_4\xi^4. \tag{60}$$

Condition 1 (no slip condition at the wall), $F(0) = 0$:

$$c_0 + s(0) + c_2(0)^2 + c_3(0)^3 + c_4(0)^4 = 0, \quad \text{or} \quad c_0 = 0. \tag{61}$$

Condition 2 (matching the freestream velocity at the boundary-layer edge), $F(1) = 1$:

$$s + c_2 + c_3 + c_4 = 1, \quad \text{or} \quad c_2 = 1 - s - c_3 - c_4. \tag{62}$$

Condition 3 (negligible shear at the boundary-layer edge), $F'(1) = 0$:

$$F'(\xi) = s + 2c_2\xi + 3c_3\xi^2 + 4c_4\xi^3, \quad \text{or} \quad F'(1) = s + 2c_2 + 3c_3 + 4c_4 = 0. \tag{63}$$

The last two expressions enable us to eliminate $c_2$ and write $c_3 = s - 2 - 2c_4$. This leaves us with the fourth requirement, Condition 4 (pressure gradient in the farfield), $F''(0) = -\Lambda$:

$$F''(\xi) = 2c_2 + 6c_3\xi + 12c_4\xi^2, \quad F''(0) = 2c_2 = -\Lambda, \quad \text{and so} \quad c_2 = -\tfrac{1}{2}\Lambda. \tag{64}$$

This value of $c_2$ may be readily substituted into the expression found through Condition 2 to retrieve $c_3 = 1 - s + \tfrac{1}{2}\Lambda - c_4$. Then, by combining $c_3$ with the expression found through Condition 3, we get $c_4 = 2s - 3 - \tfrac{1}{2}\Lambda$ and $c_3 = 4 - 3s + \Lambda$.

21

American Institute of Aeronautics and Astronautics

We thus arrive at

$$F(\xi) = s\xi - \tfrac{1}{2}\Lambda\xi^2 + (4 - 3s + \Lambda)\xi^3 + (2s - 3 - \tfrac{1}{2}\Lambda)\xi^4 \quad \text{(quartic)}, \tag{65}$$

and, using only Conditions 1, 2, and 4, we find, alternatively,

$$F(\xi) = s\xi - \tfrac{1}{2}\Lambda\xi^2 + (1 - s + \tfrac{1}{2}\Lambda)\xi^3 \quad \text{(cubic)}. \tag{66}$$

At this juncture, since flow detachment at separation implies $F'(0) = 0$, one is left with

$$s = s_0 + s_1\Lambda_{\text{sep}} = 0 \quad \text{or} \quad \Lambda_{\text{sep}} = -\frac{s_0}{s_1}, \tag{67}$$

where a two-term expansion of the velocity slope at the wall is used. In the absence of a pressure gradient, $s_0$ may be readily determined to be 3/2 (KP3), 2 (KP4), and 5/3 (MX4)[17]. The last constant, $s_1$, may be obtained from Eq. (15) (KP3) and Eq. (17) (KP4), thus leading to $s = 3/2 + \Lambda/4$ (KP3) and $s = 2 + \Lambda/6$ (KP4). As for the rationally-optimized quartic profile, one obtains $s_1$ in such a manner to minimize the $L_2$ error across the viscous domain. One obtains $s = 5/3 + (83/400)\Lambda$. We finally arrive at:

$$F(\xi) = \begin{cases} \tfrac{3}{2}\xi - \tfrac{1}{2}\xi^3 + \tfrac{1}{4}\Lambda\left(\xi - 2\xi^2 + \xi^3\right) & \text{(KP3)}, \\ 2\xi - 2\xi^3 + \xi^4 + \tfrac{1}{6}\Lambda\left(\xi - 3\xi^2 + 3\xi^3 - \xi^4\right) & \text{(KP4)}, \\ \tfrac{5}{3}\xi - \xi^3 + \tfrac{1}{3}\xi^4 + \Lambda\left(\tfrac{83}{400}\xi - \tfrac{1}{2}\xi^2 + \tfrac{151}{400}\xi^3 - \tfrac{17}{200}\xi^4\right) & \text{(MX4)}, \end{cases} \tag{68}$$

with

$$\Lambda_{\text{sep}} = \begin{cases} -6 & \text{(KP3)}, \\ -12 & \text{(KP4)}, \\ -8.0321 & \text{(MX4)}. \end{cases} \tag{69}$$

## C. Angular Variation of the Pohlhausen Pressure Parameter

This section provides the polynomial approximations that enable the user to solve for $\Lambda$ directly as a function of $\phi$ for each of the three profiles under consideration. One gets:

$$\Lambda(\phi) = 6.273919 + 0.395242\phi - 8.422234\phi^2 + 48.651031\phi^3 - 185.610093\phi^4 + 412.865334\phi^5$$
$$- 565.752359\phi^6 + 482.671630\phi^7 - 249.799142\phi^8 + 71.813531\phi^9 - 8.811819\phi^{10} \quad \text{(KP3)}, \tag{70}$$

$$\Lambda(\phi) = 7.214982 + 1.883475\phi - 32.958116\phi^2 + 218.289016\phi^3 - 789.364671\phi^4 + 1661.397226\phi^5$$
$$- 2146.640907\phi^6 + 1724.723478\phi^7 - 840.031463\phi^8 + 227.019743\phi^9 - 26.129896\phi^{10} \quad \text{(KP4)}, \tag{71}$$

and

$$\Lambda(\phi) = 6.074946 + 1.656599\phi - 29.794450\phi^2 + 197.292144\phi^3 - 723.411948\phi^4 + 1545.684314\phi^5$$
$$- 2026.622929\phi^6 + 1652.001660\phi^7 - 816.173724\phi^8 + 223.698442\phi^9 - 26.104890\phi^{10} \quad \text{(MX4)}. \tag{72}$$

## D. Normal Velocity Formulation

Beginning with the continuity relation given by Eq. (1), substituting $u = F(\xi)U(x)$, and rearranging, one gets:

$$v = -\frac{\partial}{\partial x}\int_0^y u\,\mathrm{d}y = -\frac{\partial}{\partial x}\int_0^y U(x)F(\xi)\,\mathrm{d}y. \tag{73}$$

As opposed to flat-plate analysis at zero incidence, flow over a cylinder, which is accompanied by a non-zero pressure gradient, leads to a varying farfield velocity $U(x)$. This warrants the use of Leibniz's integral rule that enables us to reduce Eq. (73) into

$$v = -\int_0^y \left[\frac{\mathrm{d}U(x)}{\mathrm{d}x}F(\xi) - U(x)\frac{\mathrm{d}F(\xi)}{\mathrm{d}x}\right]\mathrm{d}y. \tag{74}$$

22

American Institute of Aeronautics and Astronautics

Due to $F(\xi)$ not being explicitly a function of $x$ but rather $\xi = y/\delta(x)$, a chain rule can be used to recover its derivative with respect to $x$. This requires setting $dy = \delta\, d\xi$ and

$$\frac{dF(\xi)}{dx} = \frac{dF}{d\xi}\frac{d\xi}{dx} = \frac{dF}{d\xi}\frac{d[y/\delta(x)]}{dx} = -\frac{y}{\delta(x)^2}F'(\xi). \tag{75}$$

The foregoing relations can be substituted back into Eq. (74) to obtain an expression for $v$ that can be readily integrated with respect to $\xi$ for an arbitrary farfield velocity $U(x)$ and boundary-layer profile $F(\xi)$. One recovers:

$$v = \int_0^\xi \left[ \xi U(x) F'(\xi)\frac{d\delta(x)}{dx} - \frac{dU(x)}{dx}F(\xi)\delta(x) \right] d\xi. \tag{76}$$

## E. Energy Balance Equations

This section details the derivation of the integro-differential energy balance equations starting from Eq. (4). As shown by White and Majdalani [9], the wall heat flux $q_w$ can be modeled within the thermal boundary-layer by putting

$$q_w \approx \frac{\partial}{\partial x}\left[ \int_0^{\delta_T} \rho c_P u (T - T_\infty)\, dy \right] = -k_f \left.\frac{\partial T}{\partial y}\right|_{y=0} \tag{77}$$

$$\approx \delta_T \frac{\partial}{\partial x}\left[ \int_0^{\delta_T} u (T - T_\infty)\, dy \right] = -\alpha \left.\frac{\partial T}{\partial \xi_T}\right|_{\xi_T=0}, \tag{78}$$

where $\xi_T = y/\delta_T$ and $dy = \delta_T\, d\xi_T$. In order to introduce the normalized velocity and temperature profiles, straightforward algebraic manipulations can be used to obtain:

$$\delta_T \frac{\partial}{\partial x}\left[ U(x)\int_0^{\delta_T} \frac{u}{U(x)}\left(\frac{T-T_\infty}{T_w-T_\infty}\right) dy \right] = -\alpha \left.\frac{d\left(\frac{T-T_\infty}{T_w-T_\infty}\right)}{d\xi_T}\right|_{\xi_T=0}. \tag{79}$$

## References

[1] Prandtl, L., "Über Flüssigkeitsbewegungen bei sehr kleiner Reibung," *Verhandlungen des III. Internationalen Mathematiker Kongresses*, 1904, pp. 484–491.

[2] Blasius, H., "Grenzschichten in Flüssigkeiten mit kleiner Reibung," *Journal of Applied Mathematics and Mechanics (ZAMM)*, Vol. 56, 1908, pp. 1–37.

[3] von Kármán, T., "Über laminare und turbulente Reibung," *Journal of Applied Mathematics and Mechanics (ZAMM)*, Vol. 1, No. 4, January 1921, pp. 233–252. doi:10.1002/zamm.19210010401.

[4] Pohlhausen, K., "Zur näherungsweisen Integration der Differentialgleichung der laminaren Grenzschicht," *Journal of Applied Mathematics and Mechanics (ZAMM)*, Vol. 1, No. 4, January 1921, pp. 252–290. doi:10.1002/zamm.19210010402.

[5] Oleinik, O. A. and Samokhin, V. N., *Mathematical Models in Boundary Layer Theory*, CRC Press, London, 1999.

[6] Schetz, J. A. and Bowersox, R. D. W., *Boundary Layer Analysis*, AIAA Education Series, Washington, DC, 2nd ed., 2011.

[7] Pritchard, P. J. and Mitchell, J. W., *Fox and McDonald's Introduction to Fluid Mechanics*, Wiley, Hoboken, NJ, 9th ed., 2015.

[8] Schlichting, H. and Gersten, K., *Boundary-Layer Theory*, Springer-Verlag, Berlin, 9th ed., 2017.

[9] White, F. M. and Majdalani, J., *Viscous Fluid Flow*, McGraw-Hill, New York, NY, 4th ed., 2021.

[10] Cantwell, B. J., "Integral Measures of the Zero Pressure Gradient Boundary Layer Over the Reynolds Number Range $0 \le R_\tau < \infty$," *Physics of Fluids*, Vol. 33, No. 8, August 2021, pp. 085108. doi:10.1063/5.0061535.

[11] Khan, W. A., Culham, J. R., and Yovanovich, M. M., "Fluid Flow and Heat Transfer in Power-Law Fluids Across Circular Cylinders: Analytical Study," *Journal of Heat Transfer*, Vol. 128, No. 9, February 2006, pp. 870–878. doi:10.1115/1.2241747.

[12] Bujurke, N. M. and Jagadeeswar, M., "Momentum Integral Method in the Analysis of Taper-Flat Slider Bearing with Second-Order Fluid," *Journal of Applied Mathematics and Mechanics (ZAMM)*, Vol. 72, 1992, pp. 225–228. doi:10.1002/zamm.19920720309.

[13] DiMaggio, G. A., Hartfield, R. J., Majdalani, J., and Ahuja, V., "Solid Rocket Motor Internal Ballistics Using an Enhanced Surface-Vorticity Panel Technique," *Physics of Fluids*, Vol. 33, No. 10, October 2021, pp. 103613–16. doi:10.1063/5.0069075.

[14] Prabhu, A., Antani, D. L., and Aggarwal, S. K., "A Kármán-Pohlhausen Type Approximate Method for Solving Second Order Boundary Layer Equations," *5th Australasian Conference on Hydraulics and Fluid Mechanics*, January 1975.

[15] Walz, A., "Ein neuer Ansatz für das Greschwindligkeitsprofil der laminaren Reibungsschicht," *Lilienthal-Bericht*, Vol. 141, No. 8, 1941.

[16] Thwaites, B., "Approximate Calculation of the Laminar Boundary Layer," *Aeronautical Quarterly*, Vol. 1, 1949, pp. 245–280. doi:10.1017/S0001925900000184.

[17] Majdalani, J. and Xuan, L.-J., "On the Kármán Momentum-Integral Approach and the Pohlhausen Paradox," *Physics of Fluids*, Vol. 32, No. 12, December 2020, pp. 123605–20. doi:10.1063/5.0036786.

[18] d'Alembert, J. l. R., *Essai d'une Nouvelle Théorie de la Résistance des Fluides*, Chez David l'aîné, Libraire, Rue S. Jacques, à la Plume d'or, Paris, France, 1752.

[19] Xuan, L.-J. and Majdalani, J., "High-Order Point-Value Enhanced Finite Volume Method for Two-Dimensional Hyperbolic Equations on Unstructured Meshes," *Journal of Computational Physics*, Vol. 423, No. 12, December 2020, pp. 109756–24. doi:10.1016/j.jcp.2020.109756.

[20] Lecordier, J.-C., Browne, L., Le Masson, S., Dumouchel, F., and Paranthoën, P., "Control of Vortex Shedding by Thermal Effect at Low Reynolds Numbers," *Experimental Thermal and Fluid Science*, Vol. 21, No. 4, May 2000, pp. 227–237. doi:10.1016/s0894-1777(00)00007-8.

[21] Wang, A. B., Trávníček, Z., and Chia, K. C., "On the Relationship of Effective Reynolds Number and Strouhal Number for the Laminar Vortex Shedding of a Heated Circular Cylinder," *Physics of Fluids*, Vol. 12, No. 6, June 2000, pp. 1401–1410. doi:10.1063/1.870391.

[22] Williamson, C. H. K. and Miller, G. D., "Three-Dimensional Phase Dynamics in a Cylinder Wake," *Meccanica*, Vol. 29, No. 4, December 1994, pp. 411–429. doi:10.1007/bf00987576.

[23] Parnaudeau, P., Carlier, J., Heitz, D., and Lamballais, E., "Experimental and Numerical Studies of the Flow over a Circular Cylinder at Reynolds Number 3900," *Physics of Fluids*, Vol. 20, No. 8, August 2008, pp. 085101. doi:10.1063/1.2957018.

[24] Xie, J. and Xie, G., "Vortex Dynamics of Supercritical Carbon Dioxide Flow Past a Heated Circular Cylinder at Low Reynolds Numbers," *Physics of Fluids*, Vol. 34, No. 1, 2022, pp. 017111–17. doi:10.1063/5.0081567.

[25] Miozzi, M., Capone, A., Di Felice, F., Klein, C., and Liu, T., "Global and Local Skin Friction Diagnostics from TSP Surface Patterns on an Underwater Cylinder in Crossflow," *Physics of Fluids*, Vol. 28, No. 12, 2016, pp. 124101–23. doi:10.1063/1.4968525.

[26] Bouhairie, S. and Chu, V. H., "Two-Dimensional Simulation of Unsteady Heat Transfer from a Circular Cylinder in Crossflow," *Journal of Fluid Mechanics*, Vol. 570, January 2007, pp. 177–215. doi:10.1017/s0022112006002941.

[27] Sircar, A., Kimber, M., Rokkam, S., and Botha, G., "Turbulent Flow and Heat Flux Analysis from Validated Large Eddy Simulations of Flow Past a Heated Cylinder in the Near Wake Region," *Physics of Fluids*, Vol. 32, No. 12, December 2020, pp. 125119. doi:10.1063/5.0031831.

[28] Jogee, S., Prasad, B., and Anupindi, K., "Large-Eddy Simulation of Non-Isothermal Flow over a Circular Cylinder," *International Journal of Heat and Mass Transfer*, Vol. 151, April 2020, pp. 119426. doi:10.1016/j.ijheatmasstransfer.2020.119426.

[29] Zafar, F. and Alam, M. M., "Flow Structure Around and Heat Transfer from Cylinders Modified from Square to Circular," *Physics of Fluids*, Vol. 31, No. 8, August 2019, pp. 083604. doi:10.1063/1.5109693.

[30] Kwon, K. and Choi, H., "Control of Laminar Vortex Shedding behind a Circular Cylinder Using Splitter Plates," *Physics of Fluids*, Vol. 8, No. 2, February 1996, pp. 479–486. doi:10.1063/1.868801.

[31] Rajani, B., Kandasamy, A., and Majumdar, S., "Numerical Simulation of Laminar Flow past a Circular Cylinder," *Applied Mathematical Modelling*, Vol. 33, No. 3, March 2009, pp. 1228–1247. doi:10.1016/j.apm.2008.01.017.

[32] Sarwar, W. and Mellibovsky, F., "Characterization of Three-Dimensional Vortical Structures in the Wake past a Circular Cylinder in the Transitional Regime," *Physics of Fluids*, Vol. 32, No. 7, July 2020, pp. 074104. doi:10.1063/5.0011311.

[33] Jiang, H. and Cheng, L., "Large-Eddy Simulation of Flow past a Circular Cylinder for Reynolds Numbers 400 to 3900," *Physics of Fluids*, Vol. 33, No. 3, March 2021, pp. 034119. doi:10.1063/5.0041168.

[34] Khan, W. A., Culham, J. R., and Yovanovich, M. M., "Fluid Flow Around and Heat Transfer From an Infinite Circular Cylinder," *Journal of Heat Transfer*, Vol. 127, 2005, pp. 785–790. doi:10.1115/1.1924629.

[35] Kreith, F., Manglik, R. M., and Bohn, M. S., *Principles of Heat Transfer*, West Publishing Company, New York, NY, 2011.

[36] Žukauskas, A. A. and Žiugžda, J., *Heat Transfer of a Cylinder in Crossflow*, Hemisphere Publishing Corporation, Washington New York, 1985.

[37] Patankar, S. V. and Spalding, D. B., *Heat and Mass Transfer in Boundary Layers: A General Calculation Procedure*, Intertext, London, 1970.

[38] Schönauer, W., "Ein Differenzenverfahren zur Lösung der Grenzschichtgleichung für stationäre, laminare, inkompressible Strömung," *Ingenieur-Archiv*, Vol. 33, No. 3, 1964, pp. 173–189. doi:10.1007/bf00531457.

[39] Terrill, R. M., "Laminar Boundary Layer Flow with Separation with and Without Suction," *Philosophical Transactions of the Royal Society, Series A*, Vol. 253, 1960, pp. 55–100. doi:10.1098/rsta.1960.0018.

[40] Wieselsberger, C. v., "Neuere Feststellungen uber die Gesetze des Flussigkeits und Luftwiderstands," *Physikalische Zeitschrift*, Vol. 22, 1921, pp. 321.

[41] Takami, H., "Steady Two-Dimensional Viscous Flow of an Incompressible Fluid past a Circular Cylinder," *Physics of Fluids*, Vol. 12, No. 12, 1969, pp. 51–56. doi:10.1063/1.1692469.

[42] D'Alessio, S. J. D. and Dennis, S. C. R., "A Method of Domain Decomposition for Calculating the Steady Flow Past a Cylinder," *Journal of Engineering Mathematics*, Vol. 28, No. 3, May 1994, pp. 227–240. doi:10.1007/bf00058438.

[43] Giedt, W. H., "Effect of Turbulence Level of Incident Air Stream on Local Heat Transfer and Skin Friction on a Cylinder," *Journal of the Aeronautical Sciences*, Vol. 18, No. 11, November 1951, pp. 725–730. doi:10.2514/8.2092.